AD-A033 723 PENNSYLVANIA STATE UNIV UNIVERSITY PARK DEPT OF MECH--ETC F/G 21/9.2
EROSIVE BURNING STUDIES OF COMPOSITE SOLID PROPELLANTS BY THE R--ETC(U)
NOV 76 M K RAZDAN, K K KUO AF-AFOSR-2914-76
UNCLASSIFIED AFOSR-TR-76-1424 NL

1 OF 1
AD
A033723

END
DATE
FILMED
2-77

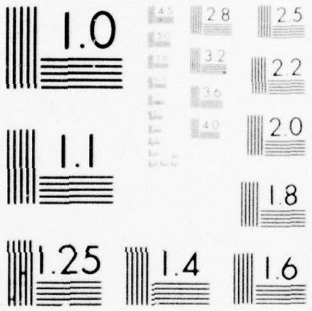

MICROCOPY RESOLUTION TEST CHART
NATIONAL BUREAU OF STANDARDS 1963 A

AFOSR - TR - 76 - 1424

③

ADA033723

1855

EROSIVE BURNING STUDIES OF COMPOSITE SOLID PROPELLANTS BY THE REACTING TURBULENT BOUNDARY-LAYER APPROACH

Interim Report
August 1, 1975 to September 30, 1976

Sponsored by
Air Force Office of Scientific Research
Bolling Air Force Base, Washington, D.C.
Grant No. AFOSR-76-2914, -2914A

Prepared by
Mohan K. Razdan and Kenneth K. Kuo

November, 1976

DDC
RECEIVED
DEC 27 1976
A

THE PENNSYLVANIA STATE UNIVERSITY
College of Engineering
Department of Mechanical Engineering
University Park, Pennsylvania

Approved for public release;
distribution unlimited.

AIR FORCE OFFICE OF SCIENTIFIC RESEARCH (AFSC)
NOTICE OF TRANSMITTAL TO DDC
This technical report has been reviewed and is
approved for public release IAW AFR 190-12 (7b).
Distribution is unlimited.
A. D. BLOSE
Technical Information Officer

AIR FORCE OFFICE OF SCIENTIFIC RESEARCH (AFSC)
NOTICE OF TRANSMITTAL TO DDC
This tech [illegible] viewed and is
approv [illegible] IAW AFR 190-12 (7b).
Distribut [illegible] is [illegible]ted.
A. D. BL[illegible]
Technical Information Officer

⑱ AFOSR ⑲ TR-76-1424

⑥ EROSIVE BURNING STUDIES OF COMPOSITE SOLID PROPELLANTS BY THE REACTING TURBULENT BOUNDARY-LAYER APPROACH .

⑨ Interim ~~Report~~, 1 Aug 75 - 30 Sep 76,
August ~~1, 1975 to September 30, 1976~~

Sponsored by
Air Force Office of Scientific Research
Bolling Air Force Base, Washington, D.C.
Grant No. AFOSR-76-2914
AFOSR-76-2914A

⑮ AF-AFOSR-2914-76

The views and conclusions contained in this document are those of the authors and should not be interpreted as necessarily representing official policies, either expressed or implied, of the Air Force Office of Scientific Research of the U.S. Government.

Prepared by
⑩ Mohan K. Razdan, telephone (814) 865-1127
Kenneth K. Kuo, telephone (814) 865-6741

⑪ Nov 76

⑯ 9711 ⑰ 01 ⑫ 82p.

Mechanical Engineering Department
The Pennsylvania State University
University Park, Pennsylvania 16802

ACCESSION for
NTIS White Section ☒
DDC Buff Section ☐
UNANNOUNCED ☐
JUSTIFICATION..........

BY..........
DISTRIBUTION/AVAILABILITY CODES
Dist. AVAIL. and/or SPECIAL
A

1473
401 929 Dn

ACKNOWLEDGEMENTS

This research has been sponsored by the Air Force Office of Scientific Research under Grant No. AFOSR-76-2914, AFOSR-76-2914A.

The project officer for this contract is Major Thomas C. Meier of the Air Force Office of Scientific Research (AFOSR) in Washington, D.C. Dr. Daweel George of the Air Force Rocket Propulsion Laboratory (AFRPL), Edwards Air Force Base in California, has supplied propellant test strips and N-4 rocket propellant grains. Their support and help is greatly appreciated.

The assistance of Mr. Carl Chambers of Redstone Arsenal who has supplied MK 125 igniters is acknowledged.

The assistance of members of the College of Engineering is also gratefully acknowledged as follows: R. L. Kovalcin and G. E. Waner, test rig design participation; J. Balogh, construction of control circuits; R. Hout[illegible] and S. Gulbernat, fabrication of the test rig.

SUMMARY

This report describes progress in the first fourteen months of research into erosive burning of composite solid propellants. Both theoretical and experimental studies were undertaken. In the theoretical study, the propellant burning process is described in a chemically reacting turbulent boundary layer formed over the propellant surface. Governing equations are formulated and the order-of-magnitude analysis of these equations is carried out, and boundary conditions are also described. Results of design calculation for test rig are presented in the section covering experimental work. The results show that various operating conditions for velocity, pressure and streamwise pressure gradient can be achieved in the test rig. Items of work to be performed in the overall program are also listed.

TABLE OF CONTENTS

NOMENCLATURE

A_s	Frequency factor in the Arrhenius Law
A_b	Propellant burning area
A_p	Piston area
C_d	Nozzle discharge coefficent
C_p	Average heat capacity of the reacting gases, $\sum_{k=1}^{N} Y_k C_{pk}$
C_{pk}	Heat capacity of the kth species
C_s	Heat capacity of solid propellant
C_v	Constant volume specific heat of gases
$\mathcal{D}$	Diffusion coefficient in Fick's Law
d_{AP}	Ammonium Perchlorate particle diameter
E_{ag}, E_{as}	Activation energies in the gas phase reaction and the solid surface decomposition
e	Internal energy of gases
F_i	Total body force in ith direction
f_{ki}	Body force of kth species in ith direction
H	Equalizer chamber height
h	Static enthalpy of gases
h_{conv}	Convective heat transfer coefficient for gases over propellant surface
h_{ign}	Static enthalpy of igniter gases
h_k	Static enthalpy of kth species
h_k°	Heat of formation of kth species
$h_{T_{exit}}$	Total enthalpy of gases at the exit
$h_{T_{spill}}$	Total enthalpy of gases at the spillage gap
$\bar{h}_k$	Reference enthalpy

$\Delta\bar{h}$	Static enthalpy difference across the boundary layer
i, j, l	Indicies representing coordinate directions 1, 2 or 3
k	Species index
k	Turbulent kinetic energy, $\frac{1}{2}(\overline{u_i' u_i'})$
k_s	Specific reaction rate constant, defined in Eq. (23)
L	Characteristic length in x-direction
Le	Lewis number, $\rho C_p D/\lambda$
M	Mass in control volume
$\dot{m}_b$	Propellant mass burning rate
$\dot{m}_{exit}$	Exit mass flow rate
$\dot{m}_{ign}$	Igniter mass flow rate
m_p	Piston mass
$\dot{m}_{spill}$	Mass flow rate through spillage gap
N	Total number of species
p	Pressure
P_{fm}	Pressure in feed mechanism chamber
Pr	Prandtl number, $C_p \mu/\lambda$
Q_L	Latent heat of vaporization for the propellant
Q_s	Heat of reaction at the propellant surface
$\dot{q}_{loss}$	Rate of heat loss
R	Gas constant
Re	Reynolds number based on L
R_u	Universal gas constant
r_b	Burning rate of solid propellant
Sc	Schmidt number, $\mu/(\rho D)$
T	Gas temperature
T_f	Flame temperature

T°	Standard reference temperature
T_{ign}	Propellant ignition temperature
T_p	Propellant temperature
T_{pi}	Propellant initial temperature
T_{ps}	Propellant surface temperature
t	Time
$\overline{U}_r$	Reference velocity of gas flow
u	Gas velocity in x-direction
u_p	Piston velocity
v	Gas velocity in y-direction
$\forall$	Volume occupied by gases
V_{ki}	Diffusion velocity of kth species in ith direction
W	Average molecular weight of gases
W_k	Molecular weight of kth species
x,y	Coordinates along and normal to propellant surface
x_p	Distance moved by piston
Y_k	Mass fraction of kth species
$\Delta\overline{Y}_k$	Change in mass fraction of kth species across the boundary layer

Greek Symbols

α_s	Propellant thermal diffusivity
δ	Boundary layer thickness
ϕ	Oxidizer-to-fuel mass ratio in solid propellant
γ	Ratio of specific heats
λ	Thermal conductivity of the gas
λ_s	Thermal conductivity of the solid propellant
μ	Viscosity of combustion gases

ν'_k, ν''_k	Stoichiometric coefficients for reactants and products
ρ	Gas density
$\bar{\rho}_r$	Reference gas density
$\Delta\bar{\rho}$	Density change across the boundary layer
ρ_s	Propellant density
ω_k	Rate change of species k due to chemical reactions
$\overline{(\ )}$	Time averaged term
$(\ )'$	Fluctuating quantity
$(\ )_{,j}$	Partial differentiation of the quantity in $(\ )$ with respect to x_j

LIST OF FIGURES

I. INTRODUCTION

Thrust and range are two important design parameters of solid propellant rocket motors. Range is determined by burning time of the propellant, and thrust as well as burning time depend on the burning rate of the propellant. In solid-propellant rocket motors, it is generally understood that burning rate is affected by a high-velocity hot combustion gas flow parallel to the propellant surface. This effect is known as erosive burning. Thus, ability to predict erosive burning effect is of prime importance in the motor design.

Propellant combustion under non-erosive burning conditions involves a large number of chemical and physical processes including change of phase, energy transfer, and mass flow. Heat transfer from the hot combustion gases to the propellant surface causes the solid propellant to vaporize into gaseous reactants. Under erosive burning conditions, the high velocity gases form a turbulent boundary layer over the propellant surface. Within the boundary layer, complex transport processes change the temperature and species distribution, and affect the chemical reaction kinetics of gaseous reaction zones. As the heat transfer rate to the propellant surface increases, more propellant vaporizes, and the gaseous mass flow rate rises, counter to direction of heat transfer. Processes of mass transfer due to blowing and convective heat transfer compete with each other and, depending on the combustion gas velocity, one dominates the other. Consequently, burning rate of a propellant in erosive burning conditions can either increase (more common) or decrease.

Erosive burning is an ever-present problem in the design of high thrust, short-burning-time solid-propellant motors. Current rocket booster designers sacrifice higher loading fraction (ratio of propellant weight to combustion chamber volume), necessary for better propulsion performance, because their knowledge of erosive burning is incomplete. Attempts to achieve higher loading fraction often cause a high pressure peak and motor failure immediately after ignition due to the erosive burning of propellant charge. If the erosive burning is serious enough and is not factored into motor design, a common consequence is unequal propellant web burnout with extended heat exposure of the chamber wall. This can also lead to chamber failure.

The current research program was undertaken to investigate theoretically and experimentally the erosive burning problem. Objectives of the research program are:

1. To advance the state-of-the-art of erosive burning processes by formulating a theoretical model describing the important physical and chemical phenomena in gaseous and solid phases.
2. To solve the theoretical model by selecting a stable, fast convergent, numerical scheme so that the effects of gas velocity, pressure gradient, and propellant physicochemical characteristics can be studied.
3. To verify the theoretical results according to the observed erosive burning phenomena under various experimental conditions for chamber pressure, gas velocity, pressure gradients, propellant ingredients, etc.
4. To develop an erosive burning rate expression which will incorporate all the important parameters known to be affecting the erosive burning phenomenon.

This report has been written to document progress toward solution of the erosive burning problem. Section II covers some of the background on erosive burning, and section III describes progress in theoretical work leading to development of governing equations, gas phase kinetics, turbulence modeling, and boundary conditions. In Section IV, experimental work related to design and fabrication of the test rig and instrumentation are discussed.

II. BACKGROUND

Erosive burning behavior has been investigated by various methods as shown in a comprehensive literature survey[1] on the erosive burning. Some important phenomena observed experimentally and effect of various parameters on erosive burning are summarized below.

Threshold Velocity: The burning rate of certain solid propellants increases only when the velocity of combustion gases (or mass velocity) is greater than a threshold velocity.[2-7] The threshold velocity has been observed to be a function of pressure.[4,5,7]

Negative Erosion: At low gas velocities (below the threshold value) many investigators have reported a decrease in the burning rate of a solid propellant compared to strand burning rate.[3-8]

Effect of Propellant Initial Temperature: An increase in the erosive burning effect due to the decrease in the propellant initial temperature has been observed.[4]

Effect of Gas Temperature: At constant gas velocity and pressure, the erosive burning rate is independent of the gas temperature.[3]

Effect of Pressure: For a given mass velocity, the erosive burning is more pronounced under lower pressures.[5,6] The influence of type of fuel and mixture ratio on the erosive burning diminishes for high pressures.[3]

Effect of Compressibility of the Caseous Stream: Erosive burning depends upon the Mach number of the convective stream.[6]

Effect of Strand Burning Rate: Low burning rate propellants experience larger erosive burning effect than high burning rate propellants, and vice versa.[2] For high burning rate propellants, prounounced threshold velocity and strong influence of gas mass velocity on the erosive burning rate have been observed.[3]

Effect of Propellant Characteristics: Erosive burning depends on the types of fuel binder and the mixture ratio in a propellant.[3,4,10]

Effect of Metal Addition: Addition of aluminum has very little effect on the erosive burning.[10,11]

Effect of Rocket Motor Length-to-Diameter Ratio: For CMDB Propellants, high pressure peaks at the head end of a rocket motor have been observed for a large length-to-diameter ratio grain.[9]

Existing theories on erosive burning can be divided into three distinct classes depending upon whether the theory is based on (a) a phenomenological heat transfer theory (without taking chemical reaction and/or flame structure into account), (b) a flame theory (a description of combustion mechanism) or (c) an aerothermochemical analysis including the considerations of heat, mass, and momentum transfer in a chemically reacting boundary layer.

Among phenomenological heat transfer theories, the Lenoir-Robillard's theory[12] is most popular. The essence of this theory is that erosive burning rate is proportional to the forced convection heat-transfer coefficient. The theory is analytical to the extent that use is made of heat-transfer correlation for transpiration-cooled surface, and empirical in the sense that the heat transfer correlation is itself empirical. Compared to experimental data, the theory supplies satisfactory agreement, which may not, however, arise from theory validity but from agreement obtained by matching the burning rate equation to the experimental data. This match is necessary to determine empirical coefficients. Utility of the Lenoir-Robillard theory is limited because the empirical coefficients must be determined experimentally for every propellant. In addition, it does not include the effect of combustion and flame structure.

The representative work on erosive burning based upon flame theory has been reported by Vandenkerckhove.[13] He considered the flame structure and the mechanism of solid phase decomposition. However, the erosive burning models utilizing combustion mechanism or flame theory concepts are handicapped by their application to special propellants, sometimes, under special flow conditions.

In erosive burning problems, most of the gaseous reactions occur within a turbulent boundary layer developed over the propellant surface by the flow of combustion gases. Therefore, the most realistic analysis of the erosive effect is the third approach which employs a description of the burning process (e.g., flame zone structure and its interaction with the flow field). Early original work of Corner[14] used Prandtl-Kármán boundary layer theory to describe the flow field. However, this work gave no consideration to the effect of mass injection, and also assumed the rate-controlling step in the solid-propellant combustion to be associated with gas-phase reaction. Modern thought asserts that such a rate-controlling step is directly affected by the decomposition pyrolysis of a solid propellant. Tsuji[15] analyzed the erosive burning of a solid propellant by the boundary-layer approximation in aerothermochemistry. He assumed a laminar boundary layer in his model but in an actual erosive burning situation the boundary layer is turbulent. His model assumed a rate-controlling step as the gas-phase chemical reaction--contrary to that of the conventional explanation of surface pyrolysis. A recent study by Razdan[16] on the erosive burning of double base solid propellants also considered a chemically reacting boundary layer approach. He also assumed laminar flow. However, Razdan's work takes into account the variation of surface temperature along the propellant grain and its effect on burning rate. Both Tsuji's and Razdan's models do not explain the negative erosive burning experienced in some propellants at low velocities.

In general, although several previous theoretical models give some insight into the mechanism of erosive burning, they inadequately describe many of the phenomena observed experimentally. For example, burning rates measured by Marklund and Lake[3] clearly show that erosive burning is affected by many parameters such as oxidizer-fuel ratio, oxidizer particle size, pressure, etc. So far, no work has been reported that incorporates the effect on erosive burning of all such important parameters. Especially, no work has been done to incorporate a sophisticated flame theory with turbulent flow processes adjacent to the burning surface.

In the current research program, the third approach mentioned above is being pursued. The most commonly used Ammonium Perchlorate (AP) composite solid propellants will be considered in the model. In order to incorporate the concepts of the burning process and the flame structure of the AP solid propellants in our theoretical model, it is very useful to review some of the non-erosive (strand) burning mechanisms.

Of many combustion models, three stand out as being comprehensive enough to lead toward a better understanding of the strand burning mechanism of AP solid propellants. They are the models of Summerfield,[17-18] Hermance,[19] and Beckstead, Derr and Price.[20]

Summerfield's Granular Diffusion Flame (GDF) Model:

The model was originally formulated by Summerfield.[17] Essential features of the two-stage GDF model are shown in Fig. 1. The model is one-

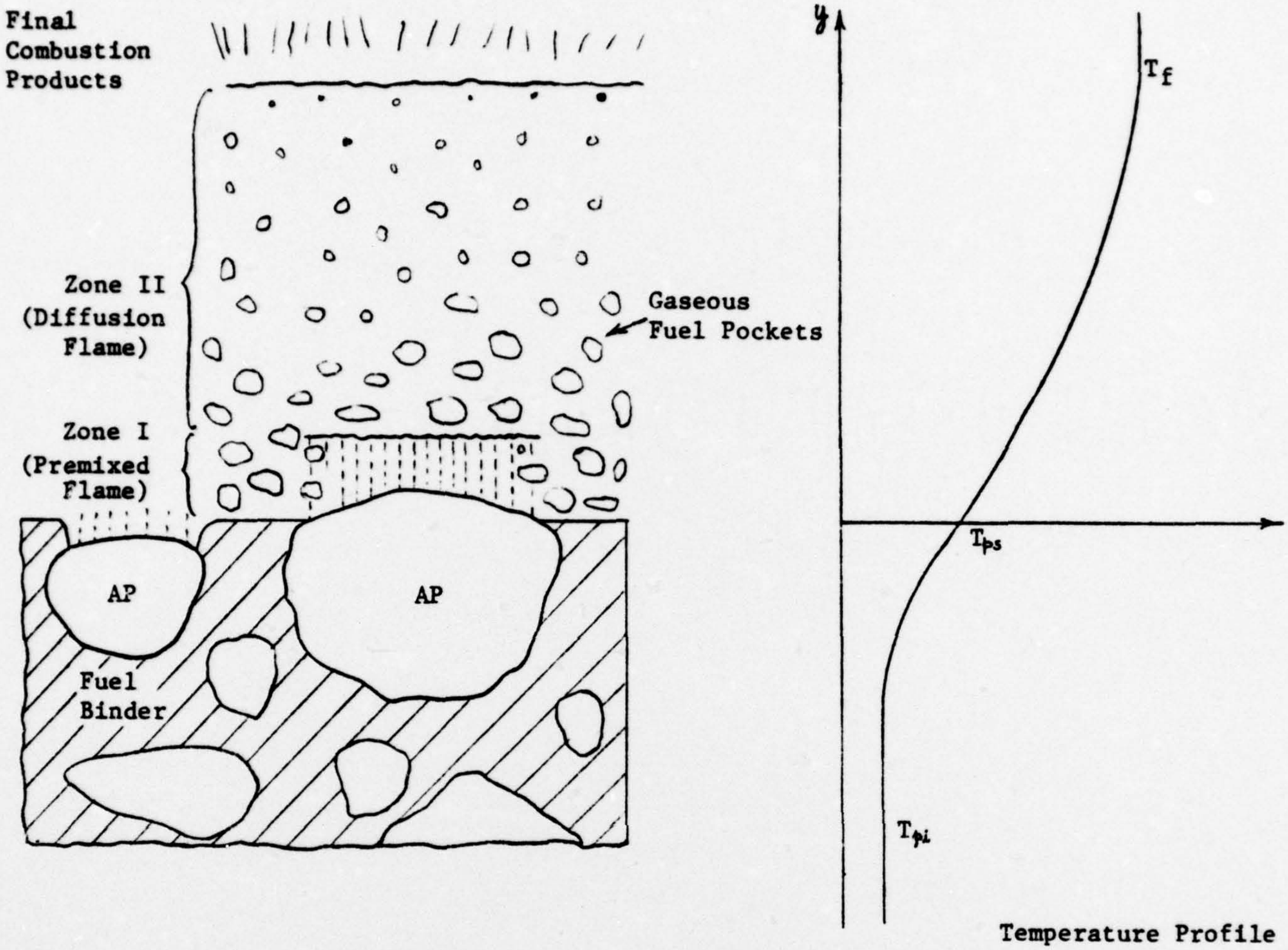

Fig. 1 TWO-STAGE GDF MODEL FOR AMMONIUM PERCHLORATE TYPE COMPOSITE SOLID PROPELLANTS (Summerfield group).[18]

THREE STEP COMPOSITE PROPELLANT BURNING:

1. Endothermic Zeroth Order Pyrolysis of Solid Fuel and Dissociative Sublimation of AP to Ammonia and Perchloric Acid.

2. Thin Premixed Exothermic $NH_3 + HClO_4$ Reaction Zone I, Assumed to Occur at the Surface for Normal Rocket Pressures. Pyrolysed Fuel Gases Are Considered Dispersed But Still Unmixed.

3. Exothermic Fuel-Oxidant Reaction, Zone II. Gaseous Fuel Pockets Are Consumed in Atmosphere of A/PA-Zone Combustion Products (Diffusionally and/or Chemical Reaction Controlled)

   BURNING RATE EXPRESSION: $1/r_b = a/p + b/p^{1/3}$

dimensional and assumes that the decomposition process at the propellant surface is controlled by the conductive heat feedback from two-stage flame occurring in the gas phase. Since composite propellant is of heterogeneous nature, the fuel and oxidizer gases emerge unmixed from the propellant surface. The model presumes that fuel enters the flame zone in tiny gas pockets. Two reaction zones, ammonia/perchloric acid (A/PA) and Fuel-oxidant, are assumed to be parallel to the propellant surface. Overall reaction rate of the fuel-oxidizer reaction is determined by rates of diffusional mixing (predominant at high pressures) and chemical reactions (predominant at low pressures). It is quite important to note that the pressure dependence of the heat feedback to the propellant surface is strongly influenced by the kinetics of the granular diffusion flame at pressures above 10 atm (even though the heat feedback from this source is considerably less than the heat contribution from A/PA reactions). The propellant burning rate relationship for this model is based on integrated, steady-state, one-dimensional energy equations for the various stations in the flame zone. The proposed burning rate equation is a function of pressure, chemical-reaction time parameter and diffusion time parameter (which in turn is a function of oxidizer particle size). These parameters are experimentally evaluated, and correlation of the burning rate equation was extremely good for a variety of propellants over the pressure range of 1 to 100 atmospheres.

Hermance's Heterogeneous Reaction Model:

The Hermance model is based on a detailed combination of the steady-state decomposition processes of the fuel and oxidizer. Three regions of propellant combustion are identified: propellant surface, the gas phase flame zone, and the region between the surface and the flame. The surface chemical processes are endothermic fuel pyrolysis, exothermic oxidizer decomposition and an exothermic heterogeneous chemical reaction between fuel binder and decomposed oxidizer in small regions surrounding individual oxidizer crystals. Each of these reactions produces a mass flux from the propellant surface. The area on which the surface reaction occurs is calculated by postulating that an oxidizer crystal decreases in size during decomposition. This size reduction produces a shallow fissure between the oxidizer crystal and the fuel binder. This fissure is the region where the heterogeneous reaction takes place. By using geometric and statistical methods, the size reduction of the oxidizer particles is expressed as a function of oxidizer volume fraction, burning rate, pressure, and oxidizer particle distribution. Although model is more detailed than GDF model, the predicted burning rates from this model were higher compared to experimental data. Further, the experimental evidence of Boggs[34] argues against the fissure postulation in this model.

The Beckstead, Derr, Price (BDP) Multiple Flame Model:

In this model the existence of three flames in the region of each exposed oxidizer particle have been postulated. Essential features of the BDP model are shown in Fig. 2. Unlike GDF model, AP monopropellant flame is considered distended from the propellant surface. Three flames considered are: (1) a primary flame between the decomposed products of the binder and the oxidizer, (2) a premixed oxidizer monopropellant flame, and (3) a final diffusion flame between the products of the oxidizer monopropellant flame and the decomposed products of the binder. Energy feedback to the propellant surface arriving from various flames is considered separately and then superimposed. For high pressures, the reaction path A in Fig. 2 is considered more important than the reaction Path B. The

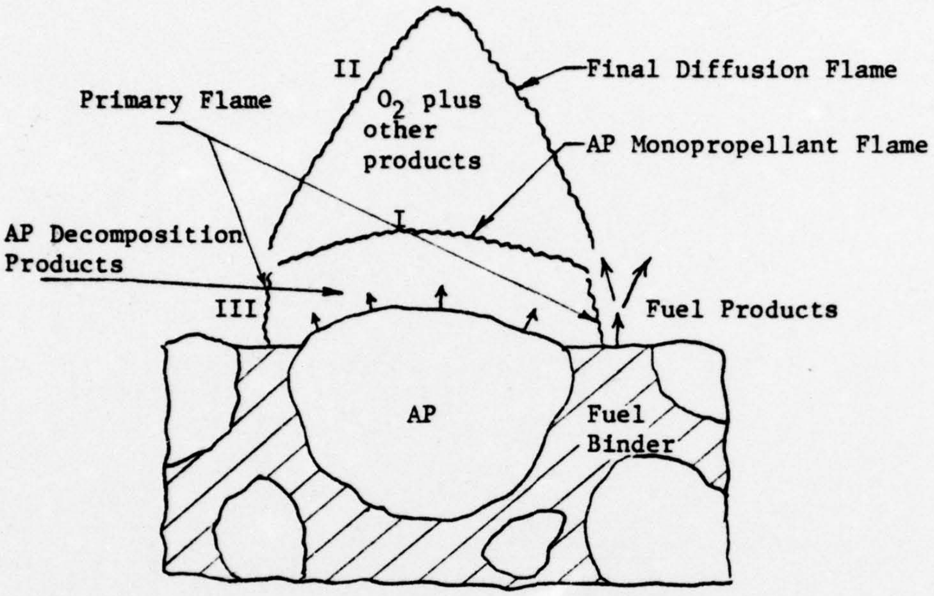

Fig. 2 POSUTLATED FLAME STRUCTURE FOR AN AP COMPOSITE PROPELLANT (BDP Model)[20]

TWO PROPOSED REACTION PATHS:

Path A:

I. AP Monopropellant Flame: $NH_3 + HClO_4$ Reaction. Independent of mixing but kinetics dependent. This flame is not considered as occuring at the surface for low pressures.

II. Final Diffusion Flame: Oxygen rich products of reaction I react with the fuel-rich binder pyrolysis products. Dependent on mixing only.

Path B:

III. Primary Flame: Fuel Pyrolysis proudcts react with $HClO_4$ products giving combustion products. Dependent on mixing and kinetics. Unimportant at high pressures.

physical nature of the oxidizer particle size and the burning surface has been described statistically, and the model is capable of describing various qualitative characteristics observed in composite propellants (e.g., plateau burning).

None of the solid propellant flame models discussed above will predict the burning rate of a composite propellant without prior knowledge of propellant combustion characteristics. In each case, various parameters in the model which are not accurately known must be varied to match the burning rate characteristics with the experimental results. Nevertheless, for the present problem, these models suggest a strong interaction of the flame zone structure with the flow field. For example, a preliminary calculation based on experimental data of references 3, 18, 21 was made and results plotted in Fig. 3. In these calculations, it has been assumed that a viscous sublayer exists and that the gas flow does not, significantly, change the diffusion flame thickness. This plot shows that the diffusion flame is outside the viscous sublayer for a high velocity combustion gas stream. It is quite evident that the role of turbulence in diffusional mixing and in rate of heat transfer to the propellant surface will be quite important in erosive burning.

The surface roughness is another factor which should be taken into account in erosive burning. At normal rocket pressures the roughness could be of the order of 10 micron.[22] This again depends on propellant formulation and in many propellants the surface roughness can be as large as the oxidizer particle size. Therefore, the Reynolds number based on the roughness size may play an important role in turbulence characteristics near the propellant surface.

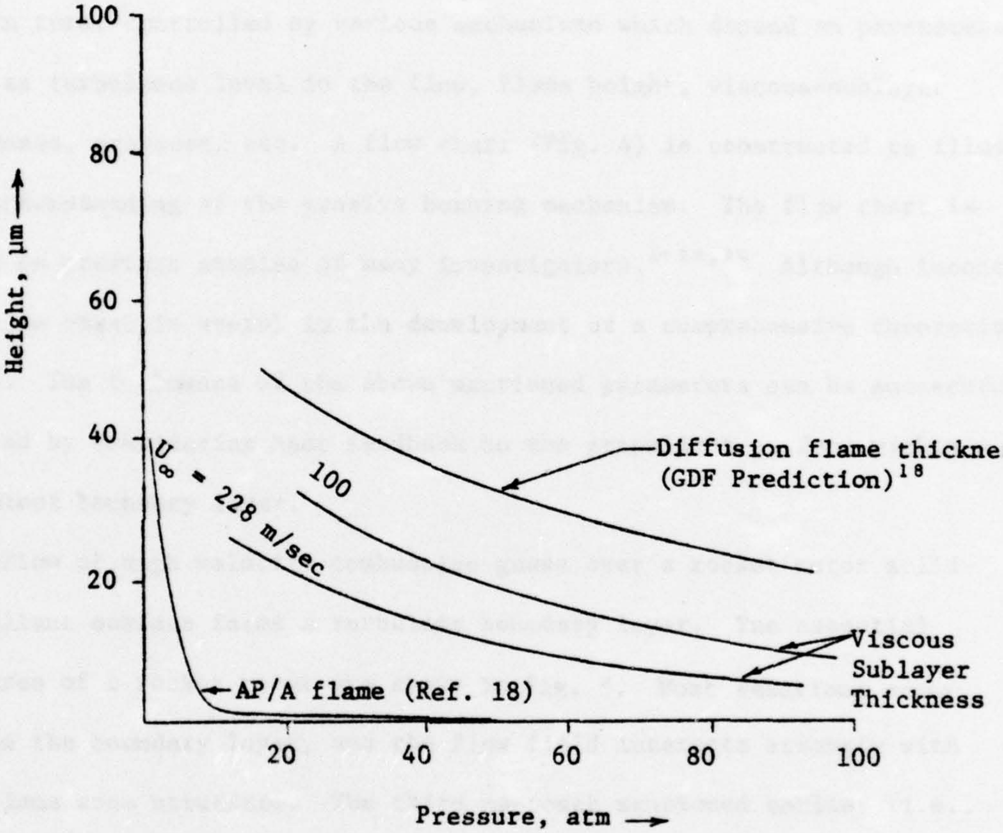

Fig. 3 Comparison of Viscous Sublayer Thickness and Diffusion Flame Thickness (viscous sublayer calculation based on experimental data on erosive burning of Ref. 3, and the data on friction coefficient of Ref. 21)

III. THEORETICAL MODELING

The burning rate of a propellant primarily depends on the rate of heat feedback from reacting gases to propellant surface. Heat feedback is, in turn, controlled by various mechanisms which depend on parameters such as turbulence level in the flow, flame height, viscous-sublayer thickness, pressure, etc. A flow chart (Fig. 4) is constructed to illustrate our understanding of the erosive burning mechanism. The flow chart is based on previous studies of many investigators.[1-20,36] Although inconclusive, the flow chart is useful in the development of a comprehensive theoretical model. The influence of the above mentioned parameters can be successfully studied by considering heat feedback to the propellant surface within a turbulent boundary layer.

Flow of high velocity combustion gases over a rocket motor solid-propellant surface forms a turbulent boundary layer. The essential features of a rocket motor are shown in Fig. 5. Most reactions occur within the boundary layer, and the flow field interacts strongly with the flame zone structure. The third approach mentioned earlier (i.e., an aerothermochemical analysis in chemically reacting turbulent boundary layer, employing a description of the burning process) is therefore the most logical analysis for the erosive burning problem. In the theoretical model, a steady, two-dimensional compressible, turbulent boundary layer over a flat plate has been considered (Fig. 6).

III.A. Governing Equations

To formulate the theoretical model, we start with the general conservation equations* for a reacting compressible fluid flow.

---

*See nomenclature for the definition of various mathematical symbols.

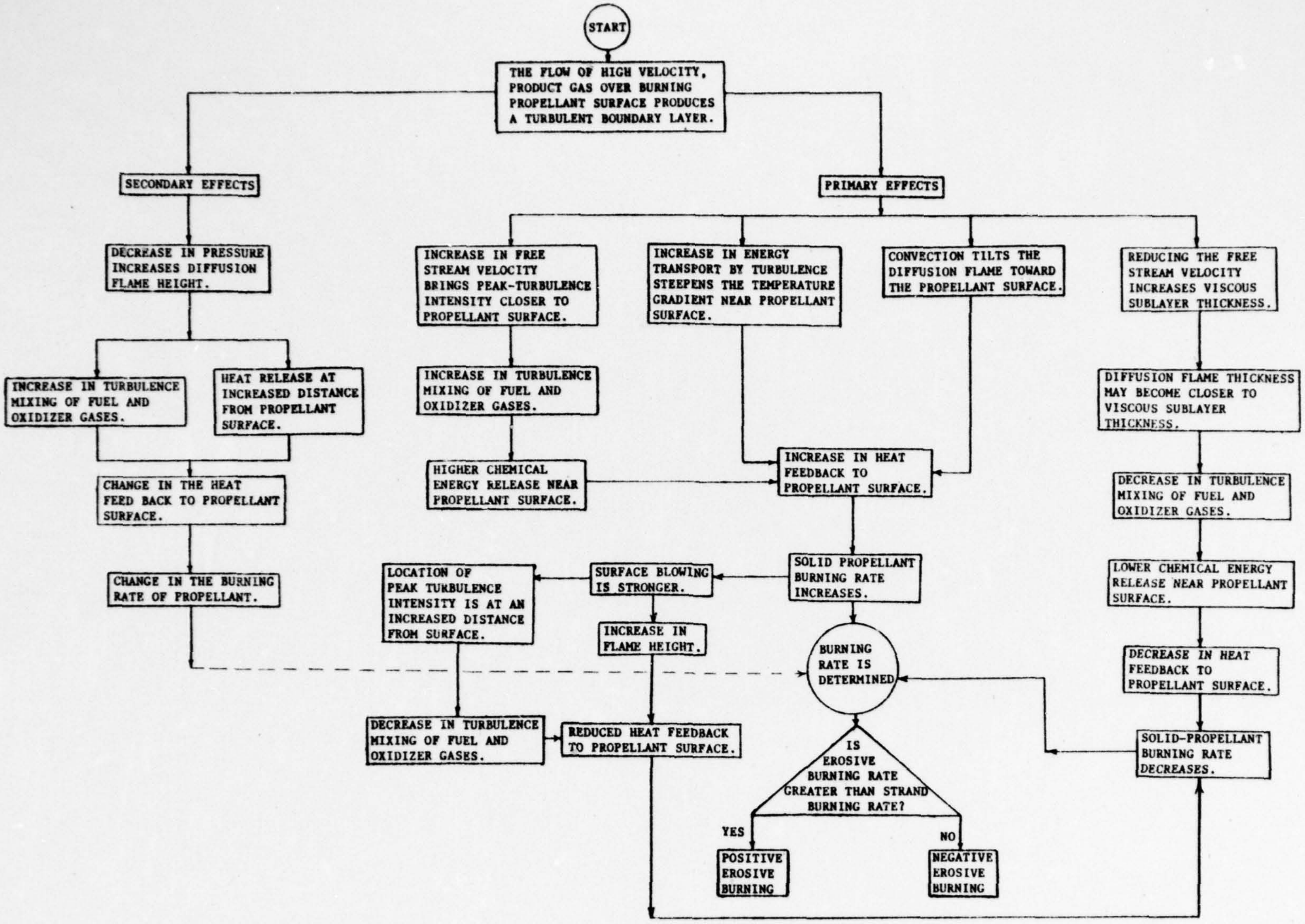

FIG. 4 FLOW CHART FOR EROSIVE BURNING MECHANISM OF COMPOSITE SOLID PROPELLANTS.

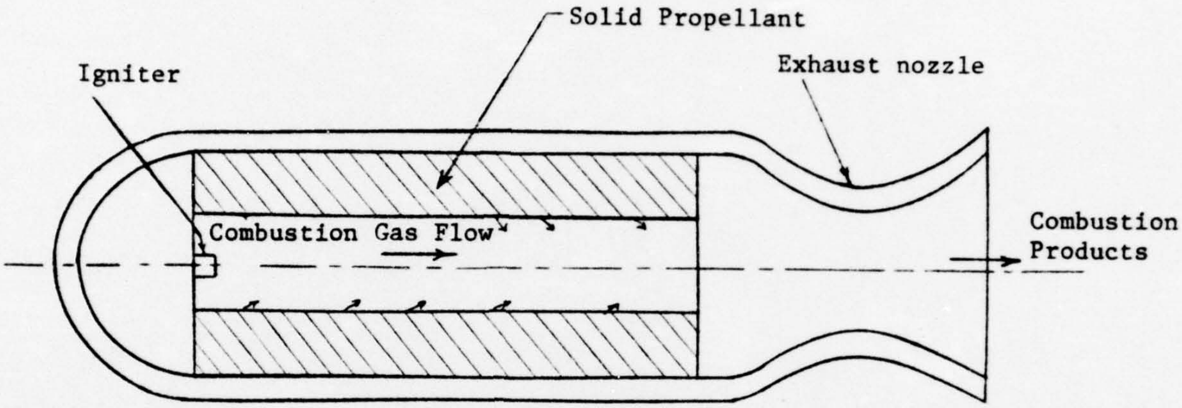

Fig. 5 Schematic Diagram of a Solid-Propellant Rocket Motor

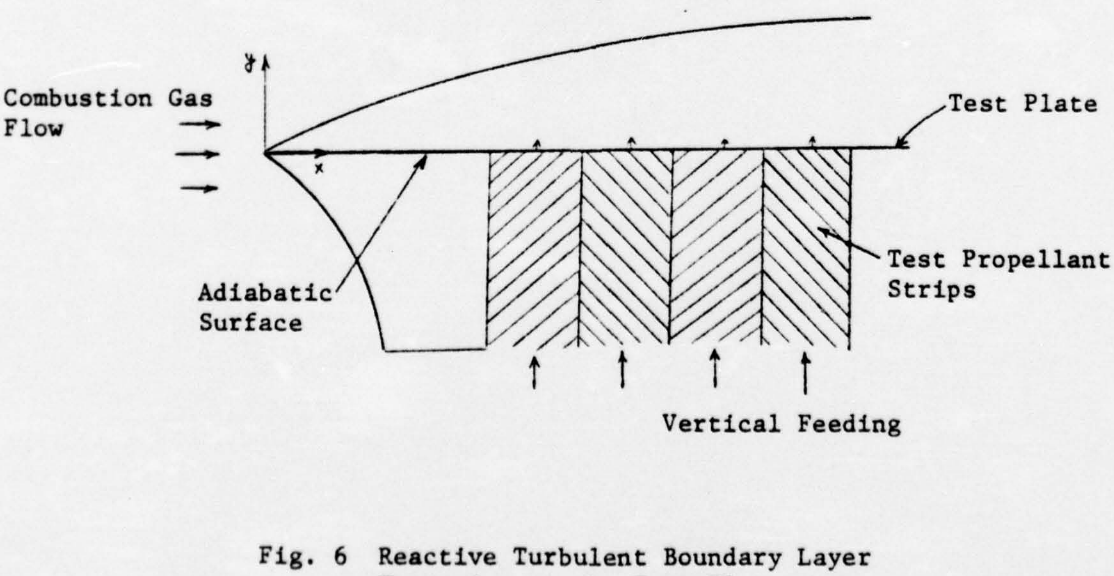

Fig. 6 Reactive Turbulent Boundary Layer Formation on the Test Plate

Mass conservation:

$$\frac{\partial \rho}{\partial t} + (\rho u_i)_{,i} = 0 \tag{1}$$

Momentum conservation:

$$\frac{\partial}{\partial t}(\rho u_i) + (\rho u_i u_j)_{,j} = -p_{,i} + \tau_{ij,j} + F_i \tag{2}$$

Species conservation:

$$\frac{\partial}{\partial t}(\rho Y_k) + (\rho Y_k u_i)_{,i} + (\rho Y_k V_{ki})_{,i} = \omega_k \quad , \quad k = 1, 2, \ldots, N \tag{3}$$

Energy conservation:

$$\frac{\partial}{\partial t}(\rho h) + (\rho u_i h)_{,i} - \frac{\partial p}{\partial t} - u_i p_{,i} = \sum_{k=1}^{N} \left\{ \left(\frac{\lambda}{C_p} Y_k h_{k,i} - \rho h_k Y_k V_{ki} \right)_{,i} + \rho Y_k f_{ki} V_{ki} \right\} + \tau_{ij} u_{i,j} \tag{4}$$

where:

$$h = \sum_{k=1}^{N} Y_k h_k \quad , \quad h_k = h_k^{\circ} + \int_{T^{\circ}}^{T} C_{p_k} \, dT \tag{5}$$

$$\tau_{ij} = \mu \left(u_{i,j} + u_{j,i} - \frac{2}{3} \delta_{ij} u_{l,l} \right) \quad , \quad \delta_{ij} = \begin{cases} 1 \text{ for } i = j \\ 0 \text{ for } i \neq j \end{cases} \tag{6}$$

Equation of state:

$$p = \rho R T \tag{7}$$

In these equations, each variable is replaced by its mean and fluctuating part (e.g., $u_i = \bar{u}_i + u_i'$, $h = \bar{h} + h'$, etc.). While doing so, the diffusion velocity, V_{ki} , appearing in equation (3) and (4) is replaced by using Fick's Law of Binary Diffusion, viz. $V_{ki} = -\frac{D}{Y_k} \frac{\partial Y_k}{\partial x_i}$. After neglecting the body force terms, each equation is averaged and the following governing equations for the mean quantities are derived:

Continuity Equation:

$$\frac{\partial \bar{\rho}}{\partial t} + (\bar{\rho} \bar{u}_i + \overline{\rho' u_i'})_{,i} = 0 \tag{8}$$

Momentum Equation:

$$\bar{\rho}\frac{\partial \bar{u}_i}{\partial t} + \frac{\partial}{\partial t}(\overline{\rho' u_i'}) + (\bar{\rho}\bar{u}_j + \overline{\rho' u_j'})\,\bar{u}_{i,j} = -\bar{p}_i + (\bar{\tau}_{i,j} - \overline{(\rho u_j)' u_i'})_{,j} \tag{9}$$

Species Equation:

$$\bar{\rho}\frac{\partial \bar{Y}_k}{\partial t} + \frac{\partial}{\partial t}\overline{\rho' Y_k'} + (\bar{\rho}\bar{u}_i + \overline{\rho' u_i'})\,\bar{Y}_{k,i} = (\bar{\rho} D \bar{Y}_{k,i} - \overline{(\rho u_i)' Y_k'})_{,i} + \bar{\omega}_k \tag{10}$$

Energy Equation:

$$\begin{aligned}
&\bar{\rho}\frac{\partial \bar{h}}{\partial t} + \frac{\partial}{\partial t}\overline{\rho' h'} + (\bar{\rho}\bar{u}_i + \overline{\rho' u_i'})\,\bar{h}_{,i} - \frac{\partial \bar{p}}{\partial t} - \bar{u}_i\bar{p}_{,i} \\
&= \left(\frac{\lambda}{c_p}\bar{h}_{,i} - \overline{(\rho u_i)' h'} + \overline{p' u_i'} + (Le-1)\sum_{k=1}^{N}\left\{\bar{h}_k\bar{Y}_{k,i} + \overline{h_k' Y_{k,i}'}\right\}\right)_{,i} \\
&\qquad + \bar{\tau}_{ij}\bar{u}_{i,j} - \overline{p' u_{i,i}'} + \overline{\tau_{ij}' u_{i,j}'}
\end{aligned} \tag{11}$$

Reynolds Stress Equation:

This equation is derived as follows: Subtract momentum equation for mean quantities from the momentum equation for instantaneous quantities and multiply by u_l'. To the resulting equation, add a similar equation with indicies i and l interchanged. Then average the whole equation, and:

$$\begin{aligned}
&\bar{\rho}\frac{\partial}{\partial t}\overline{u_i' u_l'} + \overline{\rho' u_i'}\frac{\partial \bar{u}_l}{\partial t} + \overline{\rho' u_l'}\frac{\partial \bar{u}_i}{\partial t} + \frac{\partial}{\partial t}(\overline{\rho' u_i' u_l'}) + (\bar{\rho}\bar{u}_j + \overline{\rho' u_j'})(\overline{u_i' u_l'})_{,j} \\
&+ \overline{(\rho u_j)' u_i'}\,\bar{u}_{l,j} + \overline{(\rho u_j)' u_l'}\,\bar{u}_{i,j} + (\bar{\rho}\,\overline{u_i' u_l' u_j'})_{,j} \\
&+ (\bar{u}_j\,\overline{u_i' u_l' \rho'} + \overline{u_i' u_l' \rho' u_j'} - \overline{u_i' u_l'}\;\overline{\rho' u_j'})_{,j} \\
&= -\left[(\overline{p' u_i'})_{,l} + (\overline{p' u_l'})_{,i}\right] + \overline{p'(u_{i,l}' + u_{l,i}')} + \overline{(u_l'\tau_{ij,j}' + u_i'\tau_{lj,j}')}
\end{aligned} \tag{12}$$

Boundary Layer Equations and Order of Magnitude Analysis:

Following assumptions are introduced into Eqs. (8) to (12):

1. Average quantities are steady state
2. Mean flow is two dimensional
3. For the Mach number range $\leqslant 1$

$$\frac{\overline{\mu' \frac{\partial u'}{\partial y}}}{\overline{\mu} \frac{\partial \overline{u}}{\partial y}} << 1 \quad \text{and} \quad \frac{\overline{\rho' u' v'}}{\overline{\rho}\, \overline{u' v'}} << 1$$

According to Laufer,[24] who based his conclusion on the experimental results of Kistler,[23] the density fluctuations have a kinematic rather than a dynamic effect on the turbulence.

4. There is no reaction generated turbulence[25]
5. $\frac{\Delta \overline{\rho}}{\overline{\rho}_r} \sim O(1)$
6. $Le = 1$
7. $\frac{\partial}{\partial x_j}\left(\overline{U}_j\, \overline{u'_i u'_l \rho'} + \overline{u'_i u'_l \rho' u'_j} - \overline{u'_i u'_l}\ \overline{\rho' u'_j} \right) << \overline{\rho}\, \overline{U}_j \frac{\partial}{\partial x_j} \overline{u'_i u'_l}$
8. $Re >> 1$, $\left(\frac{L}{\delta}\right)^2 \frac{1}{Re} \sim O(1)$, $\frac{\delta}{L} << 1$

Following the regular procedure for order of magnitude analysis (see Appendix A), dominant terms in the Eqs. (7) - (12) are retained. Turbulent kinetic energy equation ($i=l$) and Reynolds shear stress equation ($i=1$, $l=2$) are obtained from Eq. (12). Finally, the two dimensional steady-state turbulent boundary layer equations for a reactive turbulent compressible flow are obtained:

Continuity Equation:

$$\frac{\partial}{\partial x}(\overline{\rho}\,\overline{U}) + \frac{\partial}{\partial y}(\overline{\rho}\,\overline{v}^{\circ}) = 0 \qquad (13)$$

where

$$\overline{\rho}\,\overline{v}^{\circ} \equiv \overline{\rho}\,\overline{v} + \overline{\rho' v'}$$

Momentum Equation:

$$\overline{\rho}\,\overline{U} \frac{\partial \overline{U}}{\partial x} + \overline{\rho}\,\overline{v}^{\circ} \frac{\partial \overline{U}}{\partial y} = - \frac{d\overline{p}}{dx} + \frac{\partial}{\partial y}\left(\mu \frac{\partial \overline{U}}{\partial y} - \overline{(\rho v)' u'} \right) \qquad (14)$$

Species Equation:

$$\bar\rho\bar u\frac{\partial\bar Y_k}{\partial x}+\bar\rho\bar v^{\circ}\frac{\partial\bar Y_k}{\partial y}=\frac{\partial}{\partial y}\left[\bar\rho D\frac{\partial\bar Y_k}{\partial y}-\overline{(\rho v)'Y_k'}\right]+\bar\omega_k \tag{15}$$

Energy Equation:

$$\bar\rho\bar u\frac{\partial\bar h}{\partial x}+\bar\rho\bar v^{\circ}\frac{\partial\bar h}{\partial y}=\frac{\partial}{\partial y}\left(\frac{\lambda}{C_p}\frac{\partial\bar h}{\partial y}\right)+\frac{\partial}{\partial y}\left[-\overline{(\rho v)'h'}+\overline{p'v'}\right]+\bar u\frac{d\bar p}{dx}$$
$$+\mu\left(\frac{\partial\bar u}{\partial y}\right)^2-\overline{p'u'_{i,i}}+\overline{\tau'_{ij}u'_{i,j}} \tag{16}$$

Contribution of $\overline{p'v'}$, $\overline{p'u'_{i,i}}$ and $\overline{\tau'_{ij}u'_{i,j}}$ in Eq. (16) is generally believed to be small compared with the convection of $\bar h$ and is therefore neglected in the subsequent analysis.

Turbulent kinetic energy equation:

$$\bar\rho\bar u\frac{\partial k}{\partial x}+\bar\rho\bar v^{\circ}\frac{\partial k}{\partial y}=-\overline{(\rho v)'u'}\frac{\partial\bar u}{\partial y}+\frac{\partial}{\partial y}\left(\mu\frac{\partial k}{\partial y}\right)+\overline{p'u'_{i,i}}$$
$$-\frac{\partial}{\partial y}\left[\bar\rho\overline{\left(k+\frac{p'}{\bar\rho}\right)v'}\right]-\mu\,\overline{u'_{i,j}u'_{i,j}} \tag{17}$$

Reynolds' shear stress equation:

$$\bar\rho\bar u\frac{\partial}{\partial x}(\overline{u'v'})+\bar\rho\bar v^{\circ}\frac{\partial}{\partial y}(\overline{u'v'})=-\overline{(\rho v)'v'}\frac{\partial\bar u}{\partial y}+\frac{\partial}{\partial y}\left[\mu\frac{\partial}{\partial y}(\overline{u'v'})\right]$$
$$-\frac{\partial}{\partial y}\left[\bar\rho\overline{\left(v'^2+\frac{p'}{\bar\rho}\right)u'}\right]+\overline{p'\left(\frac{\partial u'}{\partial y}+\frac{\partial v'}{\partial x}\right)}$$
$$-2\mu\overline{\frac{\partial u'}{\partial x_j}\frac{\partial v'}{\partial x_j}} \tag{18}$$

Equation of State:

$$\bar p=\frac{\gamma-1}{\gamma}\left(\bar\rho\bar h+\overline{\rho'h'}\right) \tag{19}$$

Heat Conduction Equation in the Solid Phase:

It is assumed that the heat conduction into the solid propellant is dominant in a direction normal to the burning surface. In a coordinate system attached to the burning surface, the temperature distribution in the solid propellant at a given x location along the surface is governed by:

$$\lambda_s \frac{\partial^2 T_p}{\partial y^2} = \rho_s C_s r_b \frac{\partial T_p}{\partial y} , \qquad \text{where} \quad -\infty < y \leq 0^- \tag{20}$$

III.B. Modeling of Gas-Phase Chemical Reactions

When a composite solid propellant burns, solid fuel and oxidizer particles transform into gases. The gases may react in several steps. However, in the present work, the following single-step chemical reaction is assumed:

$$O + F \rightarrow P \tag{21}$$

where O and F represent the oxidizer and the fuel gases respectively, and P represents the product gases. In view of the already complicated turbulent transport phenomena, the above assumption is justified.

For this single-step reaction, production of kth species due to the chemical reaction is given by the following equation:

$$\omega_k = W_k (\nu_k'' - \nu_k') k_s \prod_{k=1}^{N} \left(\frac{\rho Y_k}{W_k} \right)^{\nu_k'} \tag{22}$$

where the specific reaction rate constant, k_s, is given by the Arrhenius law:

$$k_s = A \exp\left(-\frac{E_{aq}}{R_u T} \right) , \tag{23}$$

in which the frequency factor: $A = B T^n , \quad 0 \leq n \leq 1$

Usually in a homogeneous reaction B is a constant. However, for diffusion controlled gas-phase reactions of a burning solid propellant, B will not be a constant. It is assumed that, at least, B has the following functional dependence:

$$B = B(d_{AP}, \phi) \tag{24}$$

From Eq. (22), the rate of consumption of oxidizer and fuel species can be represented by:

$$\omega_o = -\frac{k_s}{W_F}\rho^2 Y_o Y_F \quad , \qquad \omega_F = -\frac{k_s}{W_o}\rho^2 Y_o Y_F$$

Applying Reynolds' decomposition to $\omega_o (= \bar{\omega}_o + \omega_o')$, and then averaging, we have:

$$\bar{\omega}_o = -\frac{k_s}{W_F}\left[\bar{\rho}^2 \bar{Y}_o \bar{Y}_F + \bar{\rho}^2 \overline{Y_o' Y_F'} + 2\bar{\rho}\bar{Y}_F \overline{\rho' Y_o'} + 2\bar{\rho}\bar{Y}_o \overline{\rho' Y_F'} + \overline{\rho'\rho'}\bar{Y}_o \bar{Y}_F\right] \tag{25}$$

A similar equation is valid for $\bar{\omega}_F$ with W_F replaced by W_o, in Eq. (25).

In the above equation, fluctuations in k_s are assumed negligible because temperature fluctuations will not introduce any significant fluctuations in k_s for large values of E_{ag} in Eq. (23). In Eq. (25), third and fourth order correlations have been neglected. It has been common to neglect all the turbulence correlations on the right hand side of Eq. (25). However, this is incorrect when the reaction rates are fast,[28] i.e., when the chemical reactions are diffusion controlled which is valid for burning composite solid propellants.

Relative importance of various correlations in Eq. (25) is currently being investigated. It is believed that the correlation $\overline{Y_o' Y_F'}$ should be related to the fuel pocket size (GDF theory), which is dominant in diffusion controlled chemical reactions.

III.C. Turbulence Closure

To solve Eqs. (13) - (19), a number of turbulence correlations (e.g., $\overline{(\rho v)' Y_k'}$, $\overline{(\rho v)' h'}$, etc.) have to be modeled. Some authors[35] have developed conservation equations for such correlations and thereby, introduced higher order correlations. The higher order correlations are usually modeled in terms of the known variables and some unknown constants. These constants, in general, are evaluated by matching the theoretical and experimental results. However, in our current approach, excess complexity is avoided in favour of simpler and faster-to-execute formulation. Also it is understood that chemical reactions in the diffusion flame play an important role in erosive burning. Therefore it would be more meaningful to describe the effects of turbulence on the chemical reactions in the closure consideration, rather than solve numerous conservation equations for higher order turbulence correlations. For the gas phase, only Eqs. (13) - (19) are treated as the governing equations in the theoretical formulation. Terms to be modeled for turbulence closure are given below.

1. Velocity diffusion terms, $\frac{\partial}{\partial x_j}(\bar{\rho}\,\overline{u_i' u_\ell' u_j'})$
2. Pressure diffusion terms, $\frac{\partial}{\partial x_\ell}(\overline{p' u_i'}) + \frac{\partial}{\partial x_i}(\overline{p' u_\ell'})$
3. Redistribution terms, $\overline{p'\left(\frac{\partial u_i'}{\partial x_\ell} + \frac{\partial u_\ell'}{\partial x_i}\right)}$
4. Dissipation terms, $\mu\,\overline{\frac{\partial u_i'}{\partial x_j}\frac{\partial u_\ell'}{\partial x_j}}$
5. Correlation appearing with Production terms, $\overline{(\rho v)' v'}$
6. Turbulence produced heat transfer, $\overline{(\rho u_i)' h'}$
7. Turbulence produced species transfer, $\overline{(\rho u_i)' Y_k'}$
8. Species correlation term, $\overline{Y_O' Y_F'}$

Currently, the modeling effort of the various terms listed above is in progress. For some of the terms, existing models of Rotta[29] and

Donaldson [28] will be examined for a possible extension to the present compressible turbulent boundary layer.

III.D. Boundary Conditions

Mass balance at the propellant surface:

Consider a thin Control Volume (C.V.) around the solid-gas interface (Fig. 7), mass balance for species k can be written as

$$\rho_s r_b Y_k\Big|_{0^-} \quad = \quad \bar{\rho}\,\bar{V}\,\bar{Y}_k\Big|_{0^+} \quad + \quad \bar{\rho}\,\bar{V}_k\,\bar{Y}_k\Big|_{0^+} \tag{26}$$

Mass Rate of kth species of solid propellant into C.V.	Mass Rate of kth Species of Gases Transported out of C.V. by surface blowing.	Mass Rate of kth Species of Gases Transported out of C.V. by diffusion.

Using $\rho_s r_b = (\bar{\rho}\bar{V})_{0^+}$ in Eq. (26), we have

$$\bar{Y}_o(x,0^+) = \frac{\bar{V}(x,0^+)}{\bar{V}(x,0^+) + \bar{V}_o(x,0^+)}\,Y_o(x,0^-) \tag{27}$$

$$\bar{Y}_F(x,0^+) = \frac{\bar{V}(x,0^+)}{\bar{V}(x,0^+) + \bar{V}_F(x,0^+)}\,Y_F(x,0^-) \tag{28}$$

Since no product species can diffuse into the solid, we have

$$Y_o(x,0^-) + Y_F(x,0^-) = 1 \tag{29}$$

$$\text{or} \quad Y_F(x,0^-) = \frac{1}{1+\phi} \tag{30}$$

Also from Fick's law, the diffusion velocity is given by

$$\bar{V}_o(x,0^+) = -\frac{D}{\bar{Y}_o(x,0^+)}\frac{\partial \bar{Y}_o}{\partial y}\Big|_{0^+} \tag{31}$$

and

$$\bar{V}_F(x,0^+) = -\frac{D}{\bar{Y}_F(x,0^+)}\frac{\partial \bar{Y}_F}{\partial y}\Big|_{0^+} \tag{32}$$

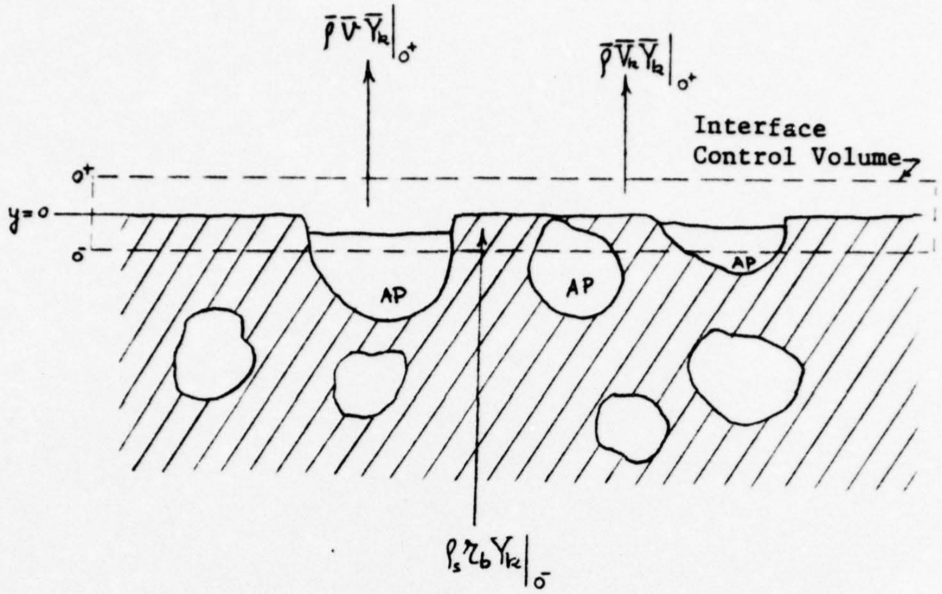

Fig. 7 Mass Balance of kth Species at the Propellant Surface

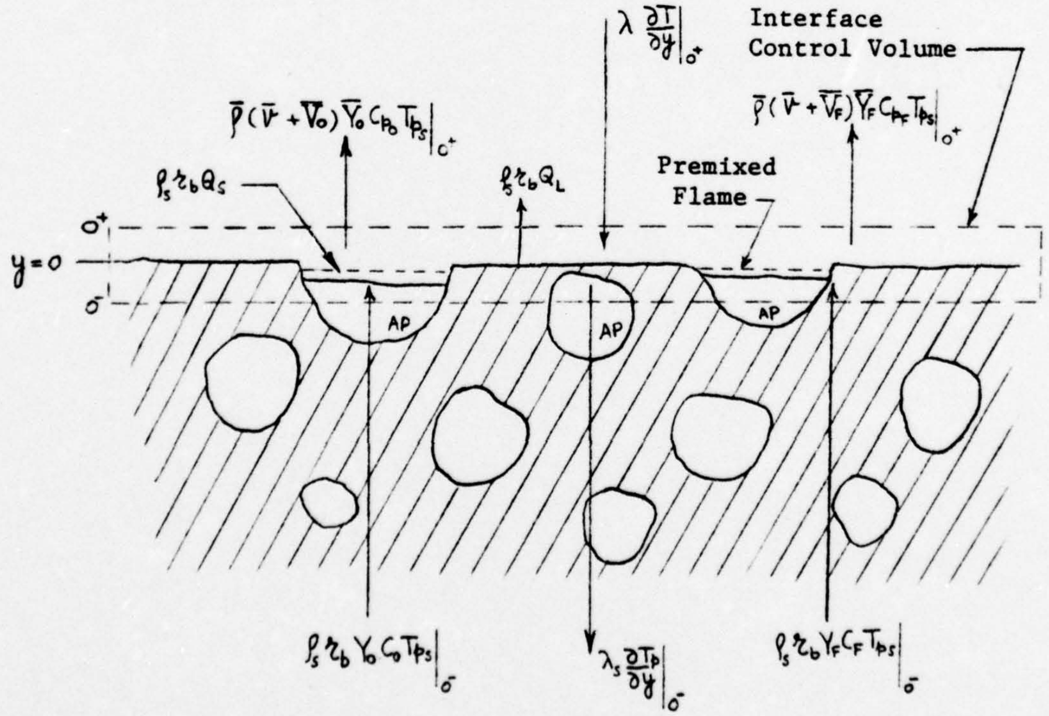

Fig. 8 Energy Balance at the Propellant Surface

Energy balance at the propellant surface:

Consider a similar solid-gas interface control volume as before; the energy balance at the propellant surface (Fig. 8) is given below.

$$\lambda_s \frac{\partial T_p}{\partial y}\bigg|_{0^-} \quad = \quad \lambda \frac{\partial \bar{T}}{\partial y}\bigg|_{0^+} \quad + \quad \rho_s r_b (Q_s - Q_L)\Big|_0$$

[Rate of Heat Flux Conducted into the Propellant.]

[Rate of Heat Feedback from gases to surface.]

[Net Rate of Heat Produced by Exothermic Reaction inside C.V.]

$$+ \; \rho_s r_b T_{ps} \left[C_o Y_o + C_F Y_F \right]\Big|_{0^-}$$

[Rate of Energy carried into the C.V. by Propellant Feeding.]

$$- \; \bar{\rho} (\bar{V} + \bar{V}_F) \bar{Y}_F C_{p_F} T_{ps}\Big|_{0^+}$$

[Rate of Energy Transported away by Convection and Diffusion of Fuel Species.]

$$- \; \bar{\rho} (\bar{V} + \bar{V}_o) \bar{Y}_o C_{p_o} T_{ps}\Big|_{0^+} \tag{33}$$

[Rate of Energy Transported away by Convection and Diffusion of Oxidizer Species.]

At the propellant surface, energy carried by convection of product species and energy carried by diffusion of product species balance each other. Therefore, there is no net contribution of product species in the energy balance equation.

Substituting Eqs. (27) and (28) into Eq. (33), and neglecting the contribution due to diffusion ($\bar{V}_k << \bar{V}$), we have:

$$\lambda_s \frac{\partial T_p}{\partial y}\bigg|_{0^-} = \lambda \frac{\partial \bar{T}}{\partial y}\bigg|_{0^+} + \rho_s r_{b(x)} \left[(Q_s - Q_L) + T_{ps(x)} (C_s - C_p) \right] \tag{34}$$

In addition to Eq. (34), the other boundary condition for the heat conduction equation in solid phase is:

$$T_p(x,-\infty) = T_{pi} \tag{35}$$

The other boundary conditions needed at the propellant surface are as follows:

$$\bar{U}(x,0) = 0 \tag{36}$$

$$\bar{V}(x,0) = \frac{\rho_s r_b(x)}{\bar{\rho}(x,0)} \tag{37}$$

where, the solid propellant burning rate is given by the Arrhenius law:

$$r_b = A_s \exp\left[-\frac{E_{as}}{R_u T_{ps}(x)}\right] \tag{38}$$

$$T(x,0) = T_{ps}(x) = T_p(x,0^-) \tag{39}$$

The boundary conditions on the adiabatic surface (Fig. 6) of the leading edge are:

$$\bar{U}(x,0^+) = 0 \tag{40}$$

$$\bar{V}(x,0^+) = 0 \tag{41}$$

$$\left.\frac{\partial T}{\partial y}\right|_{0^+} = 0 \tag{42}$$

$$\bar{Y}_o(x,0^+) = 0 \tag{43}$$

$$\bar{Y}_F(x,0^+) = 0 \tag{44}$$

The boundary conditions at the free stream are:

$$\bar{U}(x,\infty) = U_\infty(x) \tag{45}$$

$$\bar{T}(x,\infty) = T_\infty(x) \tag{46}$$

$$\bar{p}(x,\infty) = p_\infty(x) \tag{47}$$

$$\bar{Y}_o(x,\infty) = 0 \tag{48}$$

$$\bar{Y}_F(x,\infty) = 0 \tag{49}$$

To solve the differential equations for k and $\overline{u'v'}$, we also need boundary conditions on them. These boundary conditions are currently under investigation.

IV. EXPERIMENTAL WORK

The objective of this portion of the work is measurement of the burning rate of a solid propellant and study of related variables. Experimental data obtained can then be used to verify the theoretical model.

Two requirements were imposed on design of the experimental apparatus Experiments should be compatible with the theoretical model, and conditions of test propellant burning should be similar to that surrounding combustion of a typical solid propellant motor. Therefore, a propellant sample should burn at high pressures (50-100 atm), a turbulent boundary layer should be formed over the propellant sample by high velocity (100-200 m/sec) gas flow, and the propellant sample surface should be flat during combustion.

IV.A. Burning Rate Measurement

A promising method for measuring burning rate is the Laser-Photodiode servomechanism technique. It has not been broadly used in erosive burning experiments. Advantages of this technique are: the burning rates measured are instantaneous and accurate, and the results of the burning rates are directly available through an electronic recording system. The basic components used in the technique are: a He - Ne Laser, a light-sensitive photodiode, a control amplifier, a recording system and a stepper motor. Schematic diagram of the Laser-Photodiode servomechanism technique is shown in Fig. 9. As the surface of the burning solid propellant strip recedes, the laser beam (previously blocked by the propellant) is detected by the photodiode to generate a small current signal. This signal is amplified in the control amplifier, and supplied to the stepper motor,

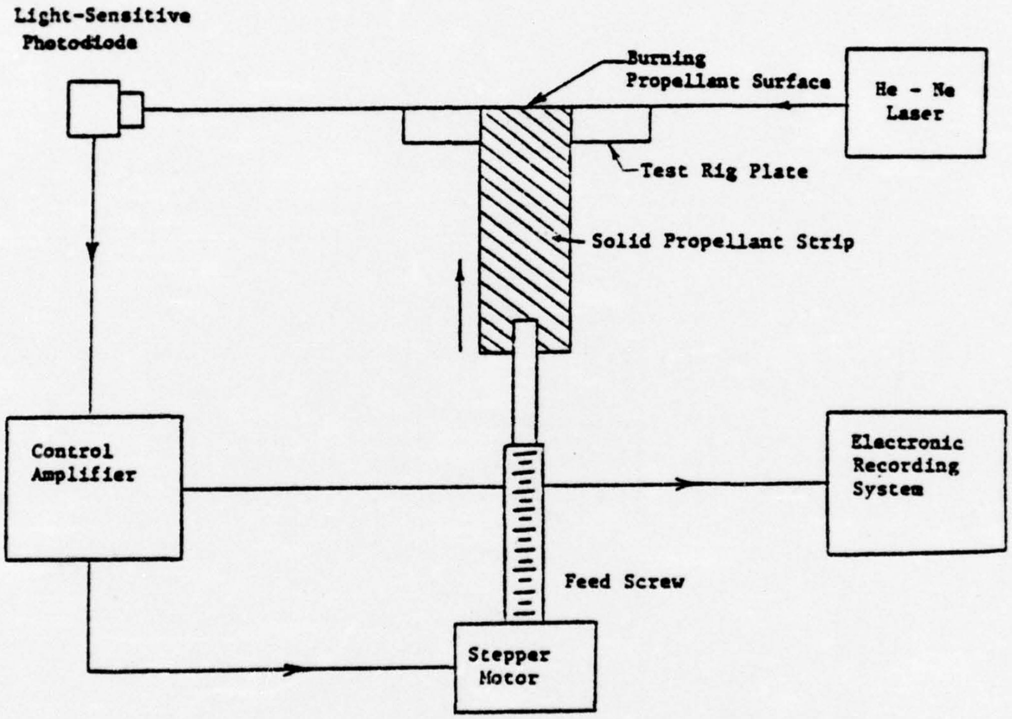

Fig. 9 Schematic Diagram of Laser-Photodiode Servomechanism for Instantaneous Burning Rate Measurements

which advances the propellant strip counter to the receding propellant surface. If the stepper motor advances the propellant too quickly, the laser beam will be blocked, the signal to the motor discontinues, and propellant strip feeding stops. Thus, feeding rate is controlled by burning rate. Both surface recession from burning and surface advancement by the stepper motor are very fast. With respect to a stationary observer, the surface of the propellant is maintained at a fixed location. The feeding rate by the stepper motor is recorded by the recording system at all times during the experiment, thus giving the instantaneous burning rate.

As mentioned earlier, a flat solid propellant surface is necessary for validation of the theory, which is modeled for a flat plate turbulent boundary layer.

When a long solid propellant surface burns in a gas stream, the surface does not regress equally at all points along the surface in the flow direction. Consequently, the surface no longer remains flat. This problem is solved by designing an experimental setup which will feed four solid propellant strips at different rates such that the flat surface is maintained. This is achieved by the experimental setup shown schematically in Fig. 10. Four laser beams together with four stepper motors control the position of the four different propellant surfaces and maintain each surface at the same level.

IV.B. Test Rig Design

The design of various components of the test rig depends on the gas dynamic operating conditions (pressure, temperature and velocity). Basic equations used for the design of the test rig are given in Appendix B. A parametric study for the effects of various geometric inputs of the test rig on the solutions of these equations is also presented in Appendix B.

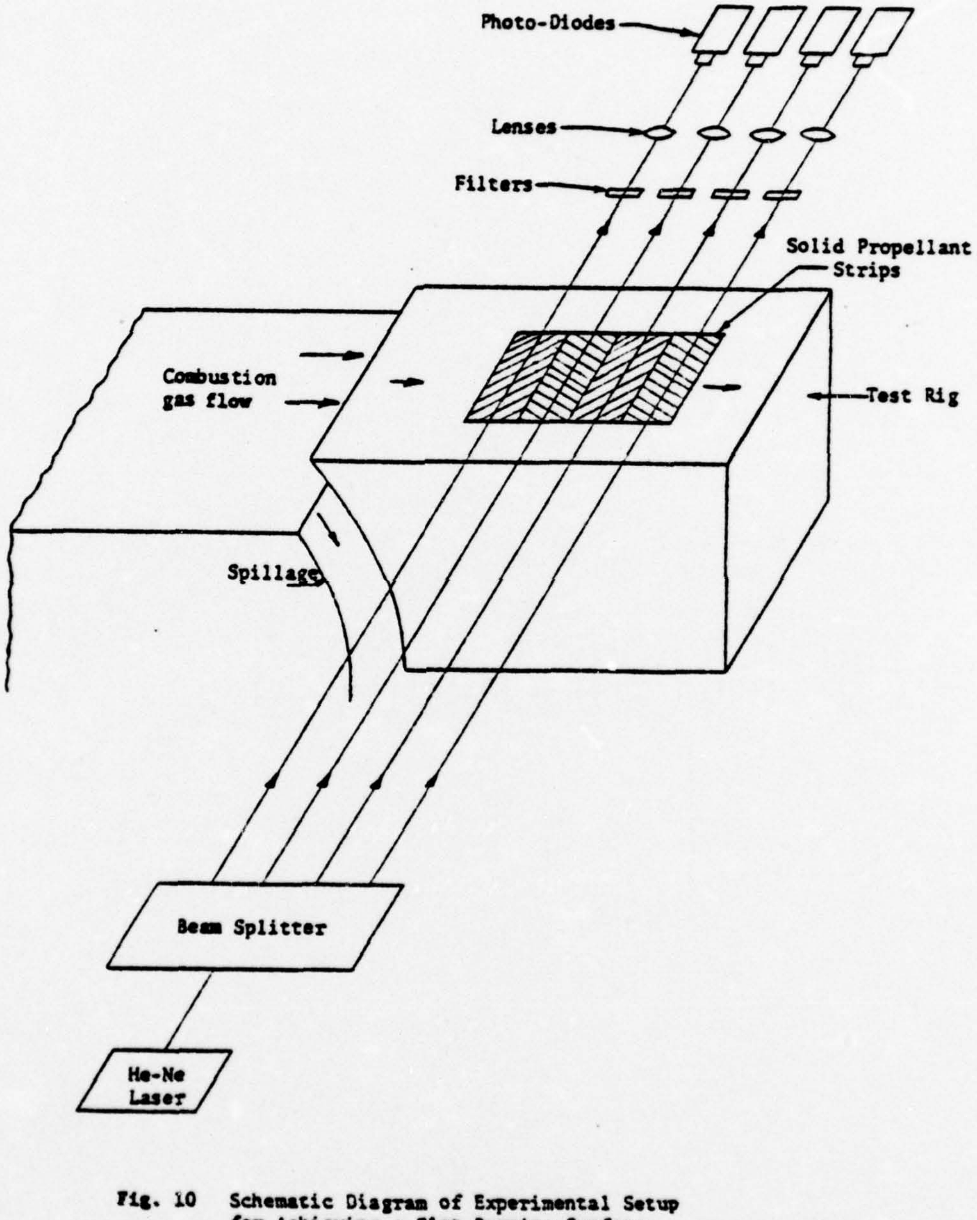

Fig. 10 Schematic Diagram of Experimental Setup for Achieving a Flat Burning Surface

Various materials and dimensions of the test rig were selected on the basis of the parametric study and the requirements of high pressure and high temperature gas flow. A schematic diagram of the test rig is shown in Fig. 11. The side (multi cross-sectional) view is shown in Fig. 12. Description and function of each important component is given below:

1. Driving Motor: For meaningful experimental results, the test conditions for the burning of propellant strips should be made similar to the burning of a propellant in a rocket motor. Consequently, a high pressure, high velocity, hot combustion gas flow is needed. Such a gas flow is generated in the driving motor by burning a 12-inch-long, star shaped, solid propellant grain. The propellant grain (N-4) is the same as used in the 5-inch sidewinder 1A motor, and has neutral burning characteristics (constant mass burning rate) which help to maintain a steady state pressure in the driving motor after a short ignition transient interval. The solid propellant grain is held in a 304 stainless steel cylindrical container, designed to withstand pressures up to 800 atm.

   To ignite the propellant charge in the driving motor, a pyrotechnic igniter (MK 125 MOD 5) which contains a mixture of black powder and magnesium, will be used. The igniter is set off by an electric squib.

   After the ignition of the propellant grain, the product gases flow out of the driving motor into the test chamber through a nozzle. This nozzle (304 stainless steel) is designed to converge from a square cross section (80 cm^2) at the end of driving motor to a rectangular cross section (20 cm^2) at the entrance of the

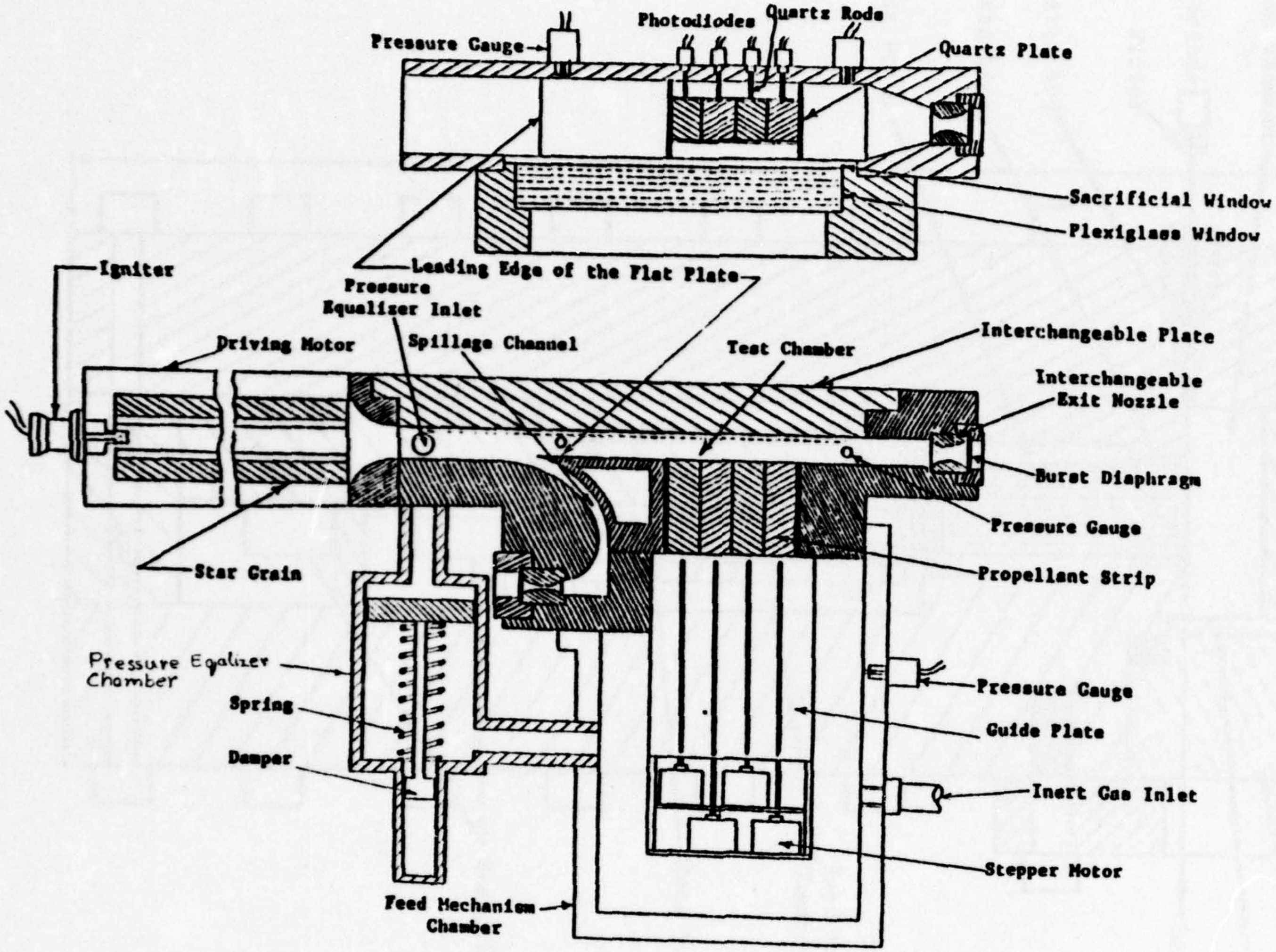

Fig.11 Schematic Diagram of the Test Rig

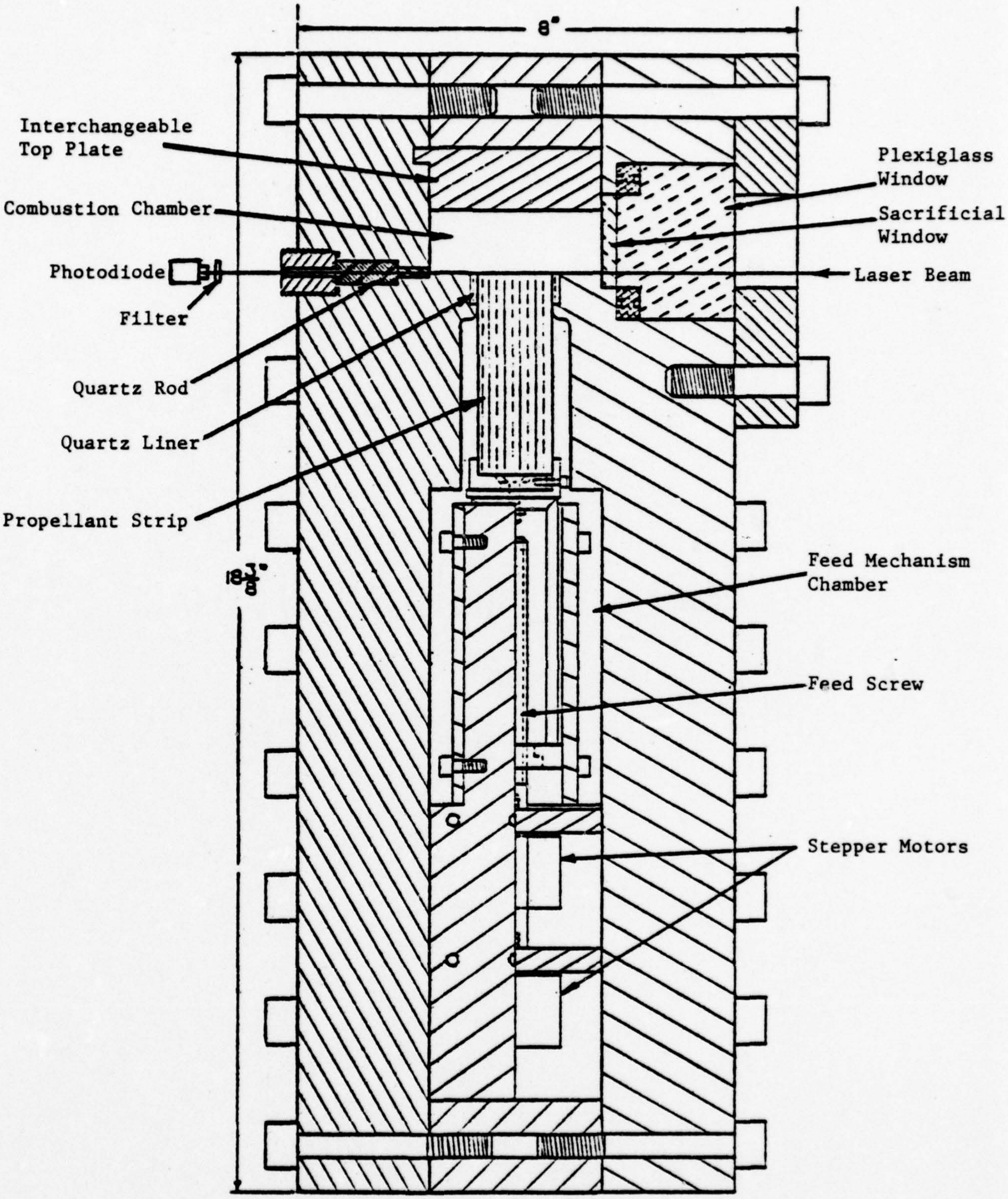

Fig. 12 Multi-Cross-Sectional Side View of the Test Rig

test chamber. To minimize the heat losses through the nozzle, the internal surface of the nozzle is coated with a thin insulation layer of zirconium oxide (Union Carbide LZ-2).

2. Test Chamber: Several important elements are designed to form the 39 cm long test chamber having a rectangular cross-section of 7 cm x 2 cm.

   The elements are described below.

   (a) An interchangeable wedge shaped stainless steel leading edge which is thermally insulated with LZ-2 coating to prevent heat losses. The leading edge is attached to a stainless steel flat plate through which four test propellant strips (7.5 cm x 3 cm x 2.5 cm) are fed by the stepper motors. The propellant strips are thermally insulated from the flat plate by using a quartz lining around the strips. This is necessary to avoid any unequal burning due to high rate of heat conduction to the propellant edges in contact with plate. The length of the leading edge (11 cm) is selected to ensure that the boundary layer is turbulent over the propellant surface.

   (b) A spillage channel through which about 10 percent of the product gases flow out of the test rig. This ensures that the boundary layer starts to develop from the beginning of the leading edge.

   (c) An interchangeable top plate is used to vary the channel height in the test section to change gas velocity. Pressure gradient can also be controlled by using a tapered top plate.

(d) A convergent-divergent interchangeable exit nozzle is designed to control the mass flow and the gas velocity in the test chamber. The exit nozzle assembly contains a burst diaphragm designed to rupture at a given critical pressure. A small nozzle with a throat area of about one tenth of the exit nozzle is used at the end of spillage channel. The small nozzle assembly also contains a burst diaphragm designed to rupture at a pressure slightly less than the critical pressure of the main exit diaphragm. This is to ensure the opening of the spillage channel. Through the use of these diaphragms, pre-pressurization of the test chamber can be achieved.

(e) A plexiglass window assembly is made of a sacrificial plexiglass plate and a main plexiglass window. This assembly is installed in the front cover of the test chamber. To enable the laser beams to pass through the test section and to be sensed by photodiodes, four small cylindrical quartz rods are located in the back plate of the test chamber.

3. Feed Mechanism Chamber: The chamber houses four stepper motors and four feed screws. Rotational motion of the feed screws (attached to the stepper motors) is converted to linear vertical motion of a rectangular element through a threaded nut (see Fig. 13). The propellant strip is carried by each of the rectangular elements. Light weight aluminum was chosen as the material for the rectangular element. Four stainless steel feed screws (3/8 in. fine SAE 24 threads/in.) are used to feed the propellant strips. The torque requirement of the stepper motor depends on: the

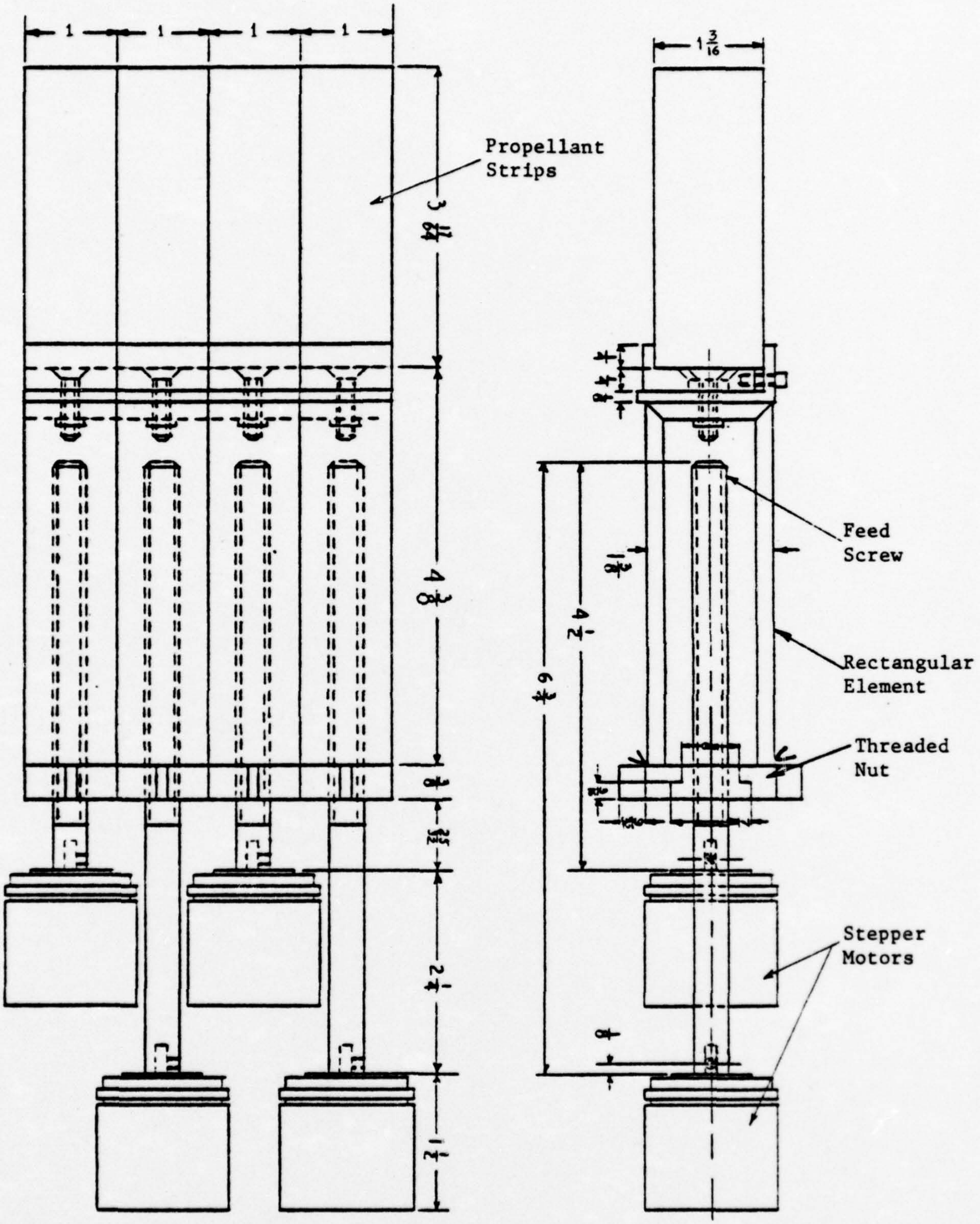

Fig. 13 Schematic Diagram of Feed Mechanism
(Dimensions in inches)

total load on the motor, friction and efficiency of the feed screw. To minimize the torque requirement of the stepper motors, the pressure difference between the test chamber and the feed mechanism chamber should be kept minimal. This is achieved by pressure equalizer chamber, discussed below.

4. Pressure Equalizer Chamber: The pressure equalizer chamber consists of a piston and a cylinder. The piston is connected with a spring and a damper to reduce oscillations of the piston. The chamber is connected to the test chamber and to the feed mechanism chamber. Higher pressure in the test chamber will push down the piston compressing the gas below it and increasing the pressure in the feed mechanism chamber. Consequently, the pressure difference between the test chamber and the feed mechanism chamber is reduced.

5. Instrumentation:

   (a) Stepper motors: A stepper motor, producing 150 pulses/sec with an index angle of 45° gives a linear feeding rate up to 2 cm/sec when 24 threads/in. screw is used. This feeding rate is within the typical values for erosive burning rates. Stepper motor control unit is used to supply the necessary voltage and current to the stepper motor. Both these items are obtained from Clifton Precision Company. The burning rate of a solid propellant strip can be measured directly by recording the feeding rate of the stepper motor.

   (b) He-Ne laser: A 6328 Å and 1-2 mw laser (Spectra-Physics model 136) is used. It has adjustable power output, precision mounting surfaces, and proper dimensions for the current design.

(c) Beam splitter: The total number of lasers needed is reduced by half by using beam splitters. These are used to split two original laser beams into four beams of equal power. Ealing Corporation's two splitter cubes having equal transmission and reflection with two reflection prisms are used for this purpose.

(d) Band-pass filter: Before the laser beam reaches a photodiode, a band-pass filter with a narrow frequency range is used to filter out any signal produced by light emission of combustion gases. The band-pass filter (Oriel Corporation model G-577-6328) having a band width of 10 Å is used for isolating the 6328 Å laser beam signal.

(e) Pressure transducers: These are used to measure the pressure at the upstream and downstream locations in the test chamber. The pressure transducers (Kistler model 601 B) having pressure range up to 1,000 atm have been selected. These transducers are equipped with water cooled adapters (Kistler Model 628 C).

(f) Thermocouple probes: Omega Engineering Tungsten - 5 percent Rhenium vs. Tungsten - 26 percent Rhenium thermocouple probes having Beryllia insulation have been selected. Temperatures up to 2600°K can be monitored.

Other instrumentation includes control amplifier, photodiodes, recording system, lead feedthroughs, laser exciters, stepper motor controls, etc.

During the reporting period, the following items have been completed as part of the experimental effort.

1. Design of the test rig has been completed, and various dimensions and materials for it have been selected, guided by analysis of various geometric inputs on gas dynamic operating condition in the test rig.
2. Fabrication of major components of the test rig has been completed.
3. Various instruments and other accessories have been selected and purchased.
4. Propellant grain for the driving motor, test-propellant strips, and pyrotechnic igniter have been acquired.
5. A four channel electronic control unit for the stepper motors has been designed and fabricated.
6. Some tests of the laser-photodiode servomechanism were conducted. Feeding mechanism and electronic integrading units operated properly, in order to record feeding rate of burning propellant strips. These same preliminary tests illustrated the feasibility of filtering light emission from burning propellant via narrow band pass filters. Laser beams can therefore be isolated and detected by photodiodes.

IV.C. Flexibility of the Experimental Apparatus

The experimental apparatus for erosive burning studies has the following flexibilities:

1. Free stream velocity and mass flux through the test chamber can be varied by changing the exit nozzle throat area and the height of the top plate in the test chamber.
2. Pressure in the test chamber can be controlled by using different exit nozzles.

3. Pressure gradients in the streamwise direction can be controlled by using a tapered interchangeable top plate.
4. Propellant strips of different compositions can be tested.

V. WORK TO BE PERFORMED

Theoretical Work

The following work is to be done in this portion of the current research program:

1. Turbulence Modeling: Modeling of the turbulence correlations listed under section III.C. is in progress. These correlations will be related in terms of known variables. Turbulence transport phenomena and the gas-phase combustion will be linked through modeling of the correlations. The boundary conditions required for the turbulence related terms (k and $\overline{u'v'}$) are also in progress. Introduction of particle size effect on erosive burning through the boundary conditions on $\overline{u'v'}$ is under consideration.
2. Numerical Solution and Parametric Studies: As soon as the theoretical formulation has been completed, three major tasks in the numerical solution will begin. The first task is selection of a stable and accurate numerical scheme. Literature survey[30-33] is already in progress to accomplish this (Crank-Nicholson implicit scheme[30] is under consideration). The second task is computer program implementation and debugging. To facilitate debugging, coding will emphasize logical simplicity rather than computational efficiency. Computational efficiency can be improved readily once program validity is established. The third task is the convergence tests and the error estimations. Convergence tests will be carried out by varying the mesh size. The solutions must change very slightly when the mesh sizes are reduced. Since convergence of numerical solutions depends upon

how well the problem is posed, various tests can be performed on solution sensitivity to changes in boundary conditions, and to changes in other important parameters such as mass flow velocity, chamber pressure, free stream temperature, initial temperature of the propellant, oxidizer particle size, oxidizer to fuel-binder ratios, and strand burning rate parameters of the propellant. In all these tests, if the solutions are bounded and change only slightly for small perturbations on the parameters, the existence of the neighboring solutions is proved, and convergence of numerical solutions is assured. Furthermore, convergence and accuracy of solutions can be verified by carrying out residual iterations, and the magnitude of the truncation errors can be determined.

Once the numerical evaluation technique is finalized, a series of "computer experiments" will be performed to determine the influence of some particular parameters of interest such as combustion gas velocity, flame temperature, pressure level, weight fraction of fuel binder, oxidizer particle size, etc. The results will be used in generating an expression for burning rate.

Experimental Work

As soon as the fabrication of the test rig has been completed, a series of experiments will be conducted. The experimental measurements will include:

1. burning rates of propellant strips,
2. mass flow rate of the combustion gases in the test chamber,

3. pressure and pressure gradient in test chamber and,
4. temperature of the combustion gases.

A high speed movie camera will be used to observe the burning process during an experimental firing.

Development of an Erosive Burning Rate Equation

Controlling dimensionless variables will be identified from the theoretical model and dimensional analysis. The variables will be measured directly or deduced indirectly from the experiments and effect of each on erosive burning will be studied experimentally. This information will be used to determine the functional form relating all the dimensionless parameters. Numerically, parametric study will be carried out to extend the range of variation of these parameters.

Measured and numerically calculated values of these parameters will be fed into a multiple-regression analysis program to determine the final correlation for erosive burning rate in terms of the non-dimensional parameters. The multiple correlation coefficient and standard deviations of the exponents and constants will be evaluated, in order to indicate the degree of correlation with experimental data. The erosive burning expression will be useful for propellant grain designers, who wish to achieve better control of erosive burning behavior in high performance rocket motors.

VI. REFERENCES

1. Kuo, K. K. and Razdan, M. K., "Review of Erosive Burning of Solid Propellants," 12th JANNAF Combustion Meeting, CPIA Publication 273, Vol. II, pp. 323-338, (1975).

2. Green, Leon, Jr., "Erosive Burning of Some Composite Solid Propellants," Jet Propulsion, Vol. 24, p. 9, (1954).

3. Marklund, T. and Lake, A., "Experimental Investigation of Propellant Erosion," ARS Journal, Vol. 3, No. 2, pp. 173-178, (1960).

4. Zucrow, M. J., Osborn, J. R. and Murphy, J. M., "An Experimental Investigation of the Erosive Burning Characteristics of a Non-Homogeneous Solid Propellant," AIAA Preprint No. 64-107, Solid Propellant Rocket Conference, Palo Alto, California, (Jan. 29-31, 1961).

5. Kreidler, J. W., "Erosive Burning: New Experimental Techniques and Methods of Analysis," AIAA Preprint No. 64-155, Solid Propellant Rocket Conference, Palo Alto, California, (Jan. 29-31, 1964).

6. Saderholm, C. A., "A Characterization of Erosive Burning for Composite H-Series Propellants," AIAA Solid Propellant Rocket Conference, Palo Alto, California, (Jan. 29-31, 1964).

7. Peretz, A., "Investigation of the Erosive Burning of Solid-Propellant Grains with Variable Port Area by Means of Interrupted Burning Experiments," Israel Journal of Technology, Vol. 3, p. 94, (1965).

8. Vilyunov, V. N. and Dvoryashin, A. A., "An Experimental Investigation of the Erosive Burning Effect," Combustion, Explosion and Shockwaves, Vol. 7, No. 1, pp. 38-42, (1971).

9. Takishita, Y., Sumi, K. and Kubota, N., "Erosive Burning Phenomena," Japan Defense Agency, Technical Research and Development Institute, (1973).

10. Lawrence, W. J. and Deverall, L. I., "The Erosive Burning Behavior of Selected Composite Propellants," 4th ICRPG Combustion Conference, Stanford, CPIA Publication No. 162, Vol. 1, pp. 459-465, (1967).

11. Dickinson, L. A., Jackson, F. and Odgers, A. L., "Erosive Burning of Polyurethane Propellants in Rocket Engines," Eighth Symposium (International) on Combustion, pp. 754-759, (1960).

12. Lenoir, J. M. and Robillard, G., "A Mathematical Method to Predict the Effects of Erosive Burning in Solid-Propellant Rockets," Sixth Symposium (International) on Combustion, pp. 663-667, (1957).

13. Vandenkerckhove, J. A., "Erosive Burning of a Colloidal Solid Propellant," Jet Propulsion, Vol. 28, pp. 599-603, (1958).

14. Corner, J., "Theory of Interior Ballistics of Guns," John Wiley and Sons, Inc., New York, (1950).

15. Tsuji, H., "An Aerothermochemical Analysis of Erosive Burning of Solid Propellant," Ninth Symposium (International) on Combustion, pp. 384-393, (1963).

16. Razdan, M. K., "Theoretical Studies on the Erosive Burning of Double-Base Solid Propellants," Master of Technology Thesis, Indian Institute of Technology, Kanpur, (June, 1974).

17. Summerfield, M., et al, "Burning Mechanism of Ammonium Perchlorate Propellants," Solid Propellant Rocket Research, p. 141, Academic Press, New York, (1960).

18. Steinz, J. A., Stang, P. L. and Summerfield, M., "The Burning Mechanism of Ammonium Perchlorate - Based Composite Solid Propellants," Aerospace and Mechanical Science Report No. 830, ONR Contract Nonr. 1858 (32), (Feb. 1969).

19. Hermance, C. E., "A Model of Composite Propellant Combustion Including Surface Heterogeneity and Heat Generation," AIAA Journal, Vol. 4, No. 9, pp. 1629-1637, (Sept. 1966).

20. Beckstead, M. W., Derr, R. L. and Price, C. F., "A Model of Composite Solid-Propellant Combustion Based on Multiple Flames," AIAA Journal, Vol. 8, No. 12, pp. 2200-2207, (Dec. 1970).

21. Squire, L. C., "The Constant Property Turbulent Boundary Layer with Injection; A reanalysis of Some Experimental Results," Int. J. Heat, Mass Transfer 13, (1970).

22. Bastress, E. K., "Modification of the Burning Rates of Ammonium Perchlorate Solid Propellants by Particle Size Control," Ph.D. Thesis, Department of Aeronautical Engineering, Princeton University, (Jan. 1961).

23. Kistler, A. L., "Fluctuation Measurement in a Supersonic Turbulent Boundary Layer," The Physics of Fluids, Vol. 2, No. 3, pp. 290-296, (May-June 1959).

24. Laufer, John, "Thought on Compressible Turbulent Boundary Layers," NASA SP-216, (Dec. 10-11, 1968).

25. Kulgein, N. G., "Transport Processes in a Compressible Turbulent Boundary Layer," Journal of Fluid Mechanics, Vol. 12, pp. 417-437, (July 1962).

26. Lin, C. C. and Shen, S. F., "A Similarity Theory for Turbulent Boundary Layer Over a Flat Plate in Compressible Flow," NACA Tech. Note 2542, (1951).

27. Herring, J. H. and Mellor, G. L., "A Method of Calculating Compressible Turbulent Boundary Layers," NASA SP-216, (Dec. 10-11, 1968).

28. Donaldson, C. duP., A Progress Report on an Attempt to Construct an Invariant Model of Turbulence Shear Flows," AGARD-CP-93, (Sept. 13-15, 1971).

29. Rotta, J. C., "Recent Attempts to Develop a Generally Applicable Calculations Method for Turbulent Shear Flow Layers," AGARD-CP-93, (Sept. 13-15, 1971).

30. Crank, J. and Nicholson, P., "A Practical Method for Numerical Integration of Solutions of Partial Differential Equations of Heat Conductions Type," Proceedings of the Cambridge Philosophical Society, Vol. 43, p. 50, (1947).

31. DuFort, E. C. and Frankel, S. P., "Stability Conditions in the Numerical Treatment of Parabolic Differential Equations," Mathematical Tables and Other Aids to Computation, Vol. 7, p. 135, (1953).

32. Patankar, S. V. and Spalding, D. B., "A Calculation Procedure for Heat, Mass and Momentum Transfer in Three-Dimensional Parabolic Flows," International Journal of Heat and Mass Transfer, Vol. 15, pp. 1787-1806, (1972).

33. Allen, J. S. and Cheng, S. I., "Numerical Solutions of the Compressible Navier-Stokes Equations for the Laminar Near Wake," The Physics of Fluids, Vol. 13, No. 1, pp. 37-52, (Jan. 1970).

34. Boggs, T. L. and Krautle, K. J., "Role of the Scanning Electron Microscope in the Study of Solid Rocket Propellant Combustion, I. Ammonium Perchlorate Decomposition and Deflegration," Combustion Science and Technology, Vol. 1, pp. 75-93, (1969).

35. Donaldson, C. duP and Varma, A. K., "Remarks on the Construction of a Second-Order Closure Description of Turbulent Reacting Flows," Combustion Science and Technology, Vol. 13, pp. 55-78, (1976).

36. Yamada, K., Goto, M. and Ishikawa, N., "A Simulative Study on the Erosive Burning of Solid Rocket Motors," AIAA Paper No. 75-1204, AIAA/SAE 11th Propulsion Conference, Anaheim, California, (Sept. 29-Oct. 1, 1975).

37. Peretz, A., Kuo, K. K., Caveny, L. H., and Summerfield, M., "Starting Transient of Solid-Propellant Rocket Motors with High Internal Gas Velocities," AIAA Journal, Vol. 11, No. 12, pp. 1719-1727, (Dec. 1973).

APPENDIX A

ORDER OF MAGNITUDE ANALYSIS

For the order of magnitude analysis of Eqs. (8) - (12), the dependable variables will be referred to their value at some reference point, r, outside the boundary layer, and coordinates x and y will be referred, respectively, by a representative dimension. Thus, we write

$$\begin{array}{ll} \bar{u} \sim \bar{U}_r & \bar{v} \sim \frac{\delta}{L}\bar{U}_r \\ \bar{\rho} \sim \bar{\rho}_r & \bar{h} \sim \bar{h}_r \\ \frac{\partial}{\partial x} \sim \frac{1}{L} & \frac{\partial}{\partial y} \sim \frac{1}{\delta} \end{array}$$

Order of magnitude of $\overline{\rho' u'}$ and $\overline{\rho' v'}$: The density fluctuations, ρ', result from several causes[26,27] listed below.

(a) Mixing of fluid elements by turbulent bulk transport from regions of different density, velocity and enthalpy.

(b) Turbulent pressure fluctuations--compressibility effect.

(c) Molecular viscous dissipation caused by fluctuating velocity and molecular heat transfer driven by the fluctuating enthalpy.

According to references 23,24,26,27, (a) is considered to be the dominant cause for production of ρ'. We, therefore, assume $\rho' \sim \ell_1 \frac{d\bar{\rho}}{dy}$, and similarly $u' \sim \ell_2 \frac{d\bar{u}}{dy}$, where ℓ_1, ℓ_2 are turbulent length scales. Assuming ℓ_1 and ℓ_2 of the same order, we get

$$\overline{\rho' u'} \simeq \overline{\rho' v'} = O\left(\overline{u'v'} \, \frac{\frac{d\bar{\rho}}{dy}}{\frac{d\bar{u}}{dy}} \right)$$

$$= O\left(\overline{u'v'} \, \frac{\frac{\Delta\bar{\rho}}{\delta}}{\frac{\bar{U}_r}{\delta}} \right)$$

$$\therefore \quad \overline{\rho' u'} \simeq \overline{\rho' v'} = O\left(\overline{u'v'}\,\frac{\Delta\bar{\rho}}{\bar{U}_r}\right) \tag{A.1}$$

From the x-momentum equation (Eq. 9), if turbulent shear stress is important, we must have

$$\frac{\partial}{\partial y}\left[\overline{(\rho v)' u'}\right] \sim O\left(\bar{\rho}\,\bar{u}\,\frac{\partial \bar{u}}{\partial x}\right)$$

But $\overline{(\rho v)' u'} \sim O(\bar{\rho}\,\overline{u'v'})$

$$\therefore \quad \frac{\partial}{\partial y}(\bar{\rho}\,\overline{u'v'}) = \left[\overline{u'v'}\,\frac{\partial \bar{\rho}}{\partial y} + \bar{\rho}\,\frac{\partial \overline{u'v'}}{\partial y}\right] \sim O\left(\bar{\rho}\,\bar{u}\,\frac{\partial \bar{u}}{\partial x}\right)$$

$$\left[\overline{u'v'}\,O\left(\frac{\Delta\bar{\rho}}{\delta}\right) + \bar{\rho}_r\,O\left(\frac{\overline{u'v'}}{\delta}\right)\right] \sim O\left(\bar{\rho}_r\,\bar{U}_r\,\frac{\bar{U}_r}{L}\right)$$

$$\overline{u'v'}\,\frac{\bar{\rho}_r}{\delta}\,O\left[1 + \frac{\Delta\bar{\rho}}{\bar{\rho}_r}\right] \sim O\left(\bar{\rho}_r\,\frac{\bar{U}_r^2}{L}\right)$$

In the present problem, temperature ratio across the boundary layer is of the order of 2 to 3, therefore

$$\frac{\Delta\bar{\rho}}{\bar{\rho}_r} \sim O(1)$$

$$\overline{u'v'} \sim O\left(\frac{\delta}{L}\,\bar{U}_r^2\right) \tag{A.2}$$

Substituting Eq. (A.2) into Eq. (A.1), we get

$$\overline{\rho' u'} \sim \overline{\rho' v'} \sim O\left(\bar{U}_r\,\Delta\bar{\rho}\,\frac{\delta}{L}\right) \tag{A.3}$$

Order of magnitude of $\overline{\rho' h'}$: Kistler[23] has found experimentally that the distribution of static temperature fluctuations is very nearly proportional to the static temperature difference across the boundary layer. Therefore, we can assume that the enthalpy fluctuations, h' , result mostly from the turbulent bulk transport of fluid elements; we can then write

$$h' \sim \ell_3 \frac{d\bar{h}}{dy}$$

Assuming the length scales ℓ_1, ℓ_2 and ℓ_3 are of the same order of magnitude, we get

$$\overline{\rho' h'} \sim O\left(\overline{u'v'} \, \frac{\frac{d\bar{\rho}}{dy} \frac{d\bar{h}}{dy}}{\frac{d\bar{u}}{dy} \frac{d\bar{u}}{dy}} \right)$$

$$\sim O\left(\frac{\delta}{L} \bar{U}_r^2 \, \frac{\frac{\Delta\bar{\rho}}{\delta} \frac{\Delta\bar{h}}{\delta}}{\frac{\bar{U}_r^2}{\delta^2}} \right)$$

$$\therefore \quad \overline{\rho' h'} \sim O\left(\Delta\bar{\rho} \Delta\bar{h} \frac{\delta}{L} \right) \tag{A.4}$$

Similarly, we can show that

$$\overline{u' h'} \sim \overline{v' h'} \sim O\left(\frac{\delta}{L} \Delta\bar{h} \, \bar{U}_r \right) \tag{A.5}$$

$$\overline{u' Y_k'} \sim \overline{v' Y_k'} \sim O\left(\frac{\delta}{L} \Delta\bar{Y}_k \bar{U}_r \right) \tag{A.6}$$

In the following, the steady state, two-dimensional conservation equations are written and the relative orders of magnitude of the terms are given below each equation.

Mass Conservation Equation:

$$\begin{array}{ccccccccc} \frac{\partial}{\partial x}(\bar{\rho}\bar{u}) & + & \frac{\partial}{\partial x}(\overline{\rho' u'}) & + & \frac{\partial}{\partial y}(\bar{\rho}\bar{v}) & + & \frac{\partial}{\partial y}(\overline{\rho' v'}) & = & 0 \\ \left(1 + \frac{\Delta\bar{\rho}}{\bar{\rho}_r}\right) & & \left(\frac{\Delta\bar{\rho}}{\bar{\rho}_r} \frac{\delta}{L}\right) & & \left(1 + \frac{\Delta\bar{\rho}}{\bar{\rho}_r}\right) & & \left(\frac{\Delta\bar{\rho}}{\bar{\rho}_r}\right) & & \end{array} \tag{A.7}$$

x-Momentum Conservation Equation:

$$\begin{array}{ccccccc} \bar{\rho}\bar{u} \frac{\partial \bar{u}}{\partial x} & + & \overline{\rho' u'} \frac{\partial \bar{u}}{\partial x} & + & \bar{\rho}\bar{v} \frac{\partial \bar{u}}{\partial y} & + & \overline{\rho' v'} \frac{\partial \bar{u}}{\partial y} \\ (1) & & \left(\frac{\Delta\bar{\rho}}{\bar{\rho}_r} \frac{\delta}{L}\right) & & (1) & & \left(\frac{\Delta\bar{\rho}}{\bar{\rho}_r}\right) \end{array}$$

$$\begin{array}{cccccccccc} = -\frac{\partial \bar{p}}{\partial x} & + \mu \Big[\frac{4}{3} \frac{\partial^2 \bar{u}}{\partial x^2} & + & \frac{1}{3} \frac{\partial^2 \bar{v}}{\partial x \partial y} & + & \frac{\partial^2 \bar{u}}{\partial y^2} \Big] & - & \frac{\partial}{\partial x} \overline{(\rho u)' u'} & - & \frac{\partial}{\partial y} \overline{(\rho v)' u'} \\ \frac{L}{\bar{\rho}_r \bar{U}_r^2} \left(\frac{\partial \bar{p}}{\partial x}\right) & \left(\frac{L}{\delta}\right)^2 \frac{1}{Re} \Big[\left(\frac{\delta}{L}\right)^2 & & \left(\frac{\delta}{L}\right)^2 & & 1 \Big] & & \left(1 + \frac{\Delta\bar{\rho}}{\bar{\rho}_r}\right) \frac{\delta}{L} & & \left(1 + \frac{\Delta\bar{\rho}}{\bar{\rho}_r}\right) \end{array} \tag{A.8}$$

y-Momentum Conservation Equation:

$$\begin{array}{cccc}
\bar{\rho}\bar{u}\frac{\partial \bar{v}}{\partial x} & + \quad \overline{\rho' u'}\,\frac{\partial \bar{v}}{\partial x} & + \quad \bar{\rho}\bar{v}\frac{\partial \bar{v}}{\partial y} & + \quad \overline{\rho' v'}\,\frac{\partial \bar{v}}{\partial y} \\
\left(\frac{\delta}{L}\right) & \left[\frac{\Delta\bar{\rho}}{\bar{\rho}_r}\left(\frac{\delta}{L}\right)^2\right] & \left(\frac{\delta}{L}\right) & \left(\frac{\Delta\bar{\rho}}{\bar{\rho}_r}\ \frac{\delta}{L}\right)
\end{array}$$

$$\begin{array}{cccccc}
= -\frac{\partial \bar{p}}{\partial y} & + \quad \mu\left[\frac{\partial^2 \bar{v}}{\partial x^2}\right. & + \quad \frac{1}{3}\frac{\partial^2 \bar{u}}{\partial x \partial y} & \left. + \quad \frac{3}{4}\frac{\partial^2 \bar{v}}{\partial y^2}\right] & - \quad \frac{\partial}{\partial x}\overline{(\rho u)' v'} & - \quad \frac{\partial}{\partial y}\overline{(\rho v)' v'} \\
\frac{L}{\bar{\rho}_r \bar{U}_r^2}\left(\frac{\partial \bar{p}}{\partial y}\right) & \left(\frac{L}{\delta}\right)^2 \frac{1}{Re}\left[\left(\frac{\delta}{L}\right)^3\right. & \left(\frac{\delta}{L}\right) & \left.\left(\frac{\delta}{L}\right)\right] & \left(1+\frac{\Delta\bar{\rho}}{\bar{\rho}_r}\right)\left(\frac{\delta}{L}\right) & \left(1+\frac{\Delta\bar{\rho}}{\bar{\rho}_r}\right)
\end{array} \tag{A.9}$$

Energy Conservation Equation:

After replacing the viscous dissipation term, $\overline{\tau}_{ij}\bar{u}_{i,j}$, by its dominant part, $\mu\left(\frac{\partial \bar{u}}{\partial y}\right)^2$, Eq. (11) becomes

$$\begin{array}{cccc}
\bar{\rho}\bar{u}\frac{\partial \bar{h}}{\partial x} & + \quad \overline{\rho' u'}\,\frac{\partial \bar{h}}{\partial x} & + \quad \bar{\rho}\bar{v}\frac{\partial \bar{h}}{\partial y} & + \quad \overline{\rho' v'}\,\frac{\partial \bar{h}}{\partial y} \\
(1) & \left(\frac{\Delta\bar{\rho}}{\bar{\rho}_r}\ \frac{\delta}{L}\right) & (1) & \left(\frac{\Delta\bar{\rho}}{\bar{\rho}_r}\right)
\end{array}$$

$$\begin{array}{cccccc}
-\bar{u}\frac{\partial \bar{p}}{\partial x} & -\bar{v}\frac{\partial \bar{p}}{\partial y} & = \quad \frac{\partial}{\partial x}\left(\frac{\lambda}{C_p}\frac{\partial \bar{h}}{\partial x}\right) & + \quad \frac{\partial}{\partial y}\left(\frac{\lambda}{C_p}\frac{\partial \bar{h}}{\partial y}\right) & - \quad \frac{\partial}{\partial x}\overline{(\rho u)' h'} \\
\left(\frac{L}{\bar{\rho}_r \Delta\bar{h}}\ \frac{\partial \bar{p}}{\partial x}\right) & \left(\frac{\delta}{L}\ \frac{L}{\bar{\rho}_r \Delta\bar{h}}\frac{\partial \bar{p}}{\partial y}\right) & \left(\frac{1}{Re\,Pr}\right) & \left[\left(\frac{L}{\delta}\right)^2\frac{1}{Re\,Pr}\right] & \left(1+\frac{\Delta\bar{\rho}}{\bar{\rho}_r}\right)\left(\frac{\delta}{L}\right)
\end{array}$$

$$\begin{array}{cc}
- \quad \frac{\partial}{\partial y}\overline{(\rho v)' h'} & + \quad \mu\left(\frac{\partial \bar{u}}{\partial y}\right)^2 \\
\left(1+\frac{\Delta\bar{\rho}}{\bar{\rho}_r}\right) & \left(\frac{L}{\delta}\right)^2\frac{1}{Re}\ \frac{\bar{U}_r^2}{\Delta\bar{h}}
\end{array} \tag{A.10}$$

Species Conservation Equation:

$$\underset{(1)}{\bar{\rho}\bar{u}\frac{\partial\bar{Y}_k}{\partial x}} + \underset{\left(\frac{\Delta\bar{\rho}}{\bar{\rho}_r}\frac{\delta}{L}\right)}{\overline{\rho' u'}\frac{\partial\bar{Y}_k}{\partial x}} + \underset{(1)}{\bar{\rho}\bar{v}\frac{\partial\bar{Y}_k}{\partial y}} + \underset{\frac{\Delta\bar{\rho}}{\bar{\rho}_r}}{\overline{\rho' v'}\frac{\partial\bar{Y}_k}{\partial y}}$$

$$= \underset{\left(\frac{1}{Re\,Sc}\right)}{\frac{\partial}{\partial x}\left(\bar{\rho}D\frac{\partial\bar{Y}_k}{\partial x}\right)} + \underset{\left[\left(\frac{L}{\delta}\right)^2\frac{1}{Re\,Sc}\right]}{\frac{\partial}{\partial y}\left(\bar{\rho}D\frac{\partial\bar{Y}_k}{\partial y}\right)} - \underset{\left(1+\frac{\Delta\bar{\rho}}{\bar{\rho}_r}\right)\left(\frac{\delta}{L}\right)}{\frac{\partial}{\partial x}\overline{(\rho u)'Y'_k}}$$

$$- \underset{\left(1+\frac{\Delta\bar{\rho}}{\bar{\rho}_r}\right)}{\frac{\partial}{\partial y}\overline{(\rho v)'Y'_k}} + \underset{\left(\frac{L}{\bar{\rho}_r\bar{U}_r\Delta\bar{Y}_k}\bar{\omega}_k\right)}{\bar{\omega}_k} \qquad \text{(A.11)}$$

Reynold's Stress Equation:

The terms $\overline{u'_\ell\tau'_{ij,j}} + \overline{u'_i\tau'_{\ell j,j}}$ of Eq. (12) can be simplified as follows

Let $[I] = \overline{u'_\ell\tau'_{ij,j}} + \overline{u'_i\tau'_{\ell j,j}}$

using $\tau'_{ij} = \mu\left(u'_{i,j} + u'_{j,i} - \frac{2}{3}\delta_{ij}u'_{m,m}\right)$

we find

$$[I] = \overline{u'_\ell(\mu u'_{i,j})_{,j}} + \overline{u'_i(\mu u'_{\ell,j})_{,j}} + \overline{u'_\ell(\mu u'_{j,i})_{,j}}$$

$$+ \overline{u'_i(\mu u'_{j,\ell})_{,j}} - \frac{2}{3}\overline{u'_\ell(\mu u'_{m,m})_{,i}}$$

$$- \frac{2}{3}\overline{u'_i(\mu u'_{m,m})_{,\ell}}$$

Let us assume (for finding relative importance of various terms in I) that μ = constant in the last four terms. Therefore, we can write

$$[I] = \frac{\partial}{\partial x_j}\left(\mu\frac{\partial\overline{u'_iu'_\ell}}{\partial x_j}\right) - 2\mu\,\overline{u'_{i,j}u'_{\ell,j}} + \frac{\mu}{3}\overline{u'_\ell u'_{j,ji}} + \frac{\mu}{3}\overline{u'_iu'_{j,j\ell}} \qquad \text{(A.12)}$$

Next, we will show that the last two terms of Eq. (A.12) are small and can be neglected. To find the order of magnitude of these two terms, differentiate the mass conservation equation of fluctuating part with respect to x_ℓ, multiply the result with u_i', and finally average the whole equation. The result is given by the following equation:

$$\overline{u_i' \frac{\partial}{\partial x_\ell}\left(\frac{\partial \rho'}{\partial t}\right)} + \bar{\rho}_{,j}\, \overline{u_i' u_{j,\ell}'} + \bar{\rho}_{,\ell}\, \overline{u_i' u_{j,j}'} + \bar{\rho}\, \overline{u_i' u_{j,j\ell}'}$$

$$+ \bar{\rho}_{,j\ell}\, \overline{u_i' u_j'} + \overline{u_i' (\rho' \bar{U}_j)_{,j\ell}} + \overline{u_i' (\rho' u_j')_{,j\ell}} = 0$$

At the most $\quad \bar{\rho}\, \overline{u_i' u_{j,j\ell}'} \backsim O\left(\bar{\rho}_{,j\ell}\, \overline{u_i' u_j'} \right)$

$$\therefore \quad \overline{u_i' u_{j,j\ell}'} \backsim O\left(\frac{\Delta \bar{\rho}}{\bar{\rho}_h} \frac{u_T^2}{\delta^2} \right)$$

Here u_T is a characteristic turbulence velocity.

Now in Eq. (A.12) $\quad \overline{u_{i,j}' u_{\ell,j}'} \backsim O\left(\frac{u_T^2}{\lambda_T^2} \right)$

where λ_T is the Taylor microscale

$$\therefore \quad \frac{\overline{u_i' u_{j,j\ell}'}}{\overline{u_{i,j}' u_{\ell,j}'}} \backsim \left(\frac{\lambda_T}{\delta}\right)^2 \frac{\Delta \bar{\rho}}{\bar{\rho}_h} << 1 , \qquad \text{because} \quad \lambda_T << \delta$$

we, therefore, can write

$$[I] = \frac{\partial}{\partial x_j}\left(\mu \frac{\partial \overline{u_i' u_\ell'}}{\partial x_j}\right) - 2\mu\, \overline{\frac{\partial u_i'}{\partial x_j} \frac{\partial u_\ell'}{\partial x_j}} \tag{A.13}$$

With this simplification and the assumption of steady state, we can write Eq. (12) into the following two equations:

Turbulent Kinetic Energy Equation: $(i = \ell)$

$$(\bar{\rho}\bar{U}_j + \overline{\rho' u_j'}) \frac{\partial k}{\partial x_j} = -\overline{(\rho u_j)' u_i'}\, \bar{U}_{i,j} + \frac{\partial}{\partial x_j}\left(\mu \frac{\partial k}{\partial x_j}\right) + \overline{p' u_{j,j}'}$$

$$- \left(\overline{\bar{\rho} k u_j' + p' u_j'}\right)_{,j} - \mu\, \overline{u_{i,j}' u_{i,j}'} \tag{A.14}$$

Reynold's Stress Equation: $(i=1, \ell=2)$

$$(\bar{\rho}\bar{u}_j + \overline{\rho' u'_j})\frac{\partial \overline{u'v'}}{\partial x_j} = -\overline{(\rho u_j)' u'}\frac{\partial \bar{v}}{\partial x_j} - \overline{(\rho u_j)' v'}\frac{\partial \bar{u}}{\partial x_j}$$

$$+ \frac{\partial}{\partial x_j}(\mu \frac{\partial \overline{u'v'}}{\partial x_j}) + \overline{p'(\frac{\partial u'}{\partial y} + \frac{\partial v'}{\partial x})} - \frac{\partial}{\partial x_j}(\bar{\rho}\overline{u'v'u'_j})$$

$$-[\frac{\partial}{\partial y}(\overline{p'u'}) + \frac{\partial}{\partial x}(\overline{p'v'})] - 2\mu\overline{\frac{\partial u'}{\partial x_j}\frac{\partial v'}{\partial x_j}} \qquad \text{(A.15)}$$

Procedure for the order of magnitude analysis of Eqs. (A.14) and (A.15) is similar to that discussed earlier. The result is that the terms with mean gradient quantities in x-direction are negligible.

After a comparison is made between the various orders of magnitude in each equation, Eq. (A.7) - (A.11), Eq. (A.14) - (A.15), only the dominant terms are retained. It is noted that

$$\frac{\delta}{L} << 1 \quad , \quad R_e >> 1$$

$$(\frac{L}{\delta})^2 \frac{1}{R_e} \leq 1 \quad , \quad P_r \sim 1 \quad , \quad S_c \sim 1$$

Finally, we obtain the following boundary layer equations for a chemically reactive, compressible, turbulent boundary layer developed over a flat plate:

Continuity Equation:

$$\frac{\partial}{\partial x}(\bar{\rho}\bar{u}) + \frac{\partial}{\partial y}(\bar{\rho}\bar{v}^{\circ}) = 0$$

$$\text{where} \quad \bar{\rho}\bar{v}^{\circ} \equiv \bar{\rho}\bar{v} + \overline{\rho' v'} \qquad \text{(A.16)}$$

Momentum Equation:

$$\bar{\rho}\bar{u}\frac{\partial \bar{u}}{\partial x} + \bar{\rho}\bar{v}^{\circ}\frac{\partial \bar{u}}{\partial y} = -\frac{d\bar{p}}{dx} + \frac{\partial}{\partial y}[\mu\frac{\partial \bar{u}}{\partial y} - \overline{(\rho v)' u'}] \qquad \text{(A.17)}$$

Species Equation:

$$\bar{\rho}\bar{u}\frac{\partial \bar{Y}_k}{\partial x} + \bar{\rho}\bar{v}^{\circ}\frac{\partial \bar{Y}_k}{\partial y} = \frac{\partial}{\partial y}\left[\bar{\rho}D\frac{\partial \bar{Y}_k}{\partial y} - \overline{(\rho v)'Y_k'}\right] + \bar{\omega}_k \qquad \text{(A.18)}$$

Energy Equation:

$$\bar{\rho}\bar{u}\frac{\partial \bar{h}}{\partial x} + \bar{\rho}\bar{v}^{\circ}\frac{\partial \bar{h}}{\partial y} = \frac{\partial}{\partial y}\left[\frac{\lambda}{c_p}\frac{\partial \bar{h}}{\partial y} + (Le-1)\sum_{k=1}^{N}\bar{h}_k\frac{\partial \bar{Y}_k}{\partial y}\right] + \bar{u}\frac{d\bar{p}}{dx} + \mu\left(\frac{\partial \bar{u}}{\partial y}\right)^2$$

$$+ \frac{\partial}{\partial y}\left[-\overline{(\rho v)'h'} + \overline{p'v'}\right] - \overline{p'u_{i,i}'} + \overline{\tau_{ij}'u_{i,j}'} \qquad \text{(A.19)}$$

Turbulent Kinetic Energy Equation:

$$\bar{\rho}\bar{u}\frac{\partial k}{\partial x} + \bar{\rho}\bar{v}^{\circ}\frac{\partial k}{\partial y} = -\overline{(\rho v)'u'}\frac{\partial \bar{u}}{\partial y} + \frac{\partial}{\partial y}\left(\mu\frac{\partial k}{\partial y}\right) + \overline{p'u_{i,i}'}$$

$$- \frac{\partial}{\partial y}\left[\overline{\bar{\rho}\left(k' + \frac{p'}{\bar{\rho}}\right)v'}\right] - \mu\,\overline{u_{i,j}'u_{i,j}'} \qquad \text{A.20)}$$

Reynolds' Shear Stress Equation:

$$\bar{\rho}\bar{u}\frac{\partial}{\partial x}(\overline{u'v'}) + \bar{\rho}\bar{v}^{\circ}\frac{\partial}{\partial y}(\overline{u'v'}) = -\overline{(\rho v)'v'}\frac{\partial \bar{u}}{\partial y} + \frac{\partial}{\partial y}\left[\mu\frac{\partial}{\partial y}(\overline{u'v'})\right]$$

$$- \frac{\partial}{\partial y}\left[\overline{\bar{\rho}\left(v'^2 + \frac{p'}{\bar{\rho}}\right)u'}\right] + \overline{p'\left(\frac{\partial u'}{\partial y} + \frac{\partial v'}{\partial x}\right)}$$

$$- 2\mu\,\overline{\frac{\partial u'}{\partial x_j}\frac{\partial v'}{\partial x_j}} \qquad \text{(A.21)}$$

APPENDIX B

BASIC EQUATIONS AND PARAMETRIC STUDIES IN THE TEST RIG DESIGN

The test rig consists of four major components: the driving motor, the test chamber, the feed mechanism chamber and the pressure equalizer chamber (see Fig. B.1). The design of these components of the test rig depends on the gas dynamic operating conditions for pressure, temperature and velocity required in the test chamber. Therefore, the equations of mass and energy balance in the driving motor and the test chamber are considered. Through these equations, the effect of various geometric inputs of the test rig on the gas dynamic operating condition can be studied.

The equations for mass and energy balance in the driving motor and the test chamber can be derived by considering a control volume in each of these components, and introducing the following assumptions:

1. All the properties are functions of time only, and
2. Perfect gas law is valid.

Mass balance in the driving motor:

$$\left(\frac{dM}{dt}\right)_d = \dot{m}_{ign} + (\dot{m}_b)_d - (\dot{m}_{exit})_d \tag{B.1}$$

Energy balance in the driving motor:

$$\left\{\frac{d(Me)}{dt}\right\}_d = \dot{m}_{ign} h_{ign} + (\dot{m}_b C_p T_f)_d - (\dot{m}_{exit} h_{T exit})_d - (\dot{q}_{r loss})_d \tag{B.2}$$

where the subscript d refers to the driving motor.

$$\left.\begin{array}{ll} \text{using} & M = \rho \forall \\ \text{and perfect gas law} & p = \dfrac{\rho R_u T}{W} \quad , \quad e = C_v T \end{array}\right\} \tag{B.3}$$

we find,

$$\frac{dM}{dt} = \rho \frac{d\forall}{dt} + \frac{\forall}{RT} \frac{dp}{dt} - \frac{\forall \rho}{T} \frac{dT}{dt} \tag{B.4}$$

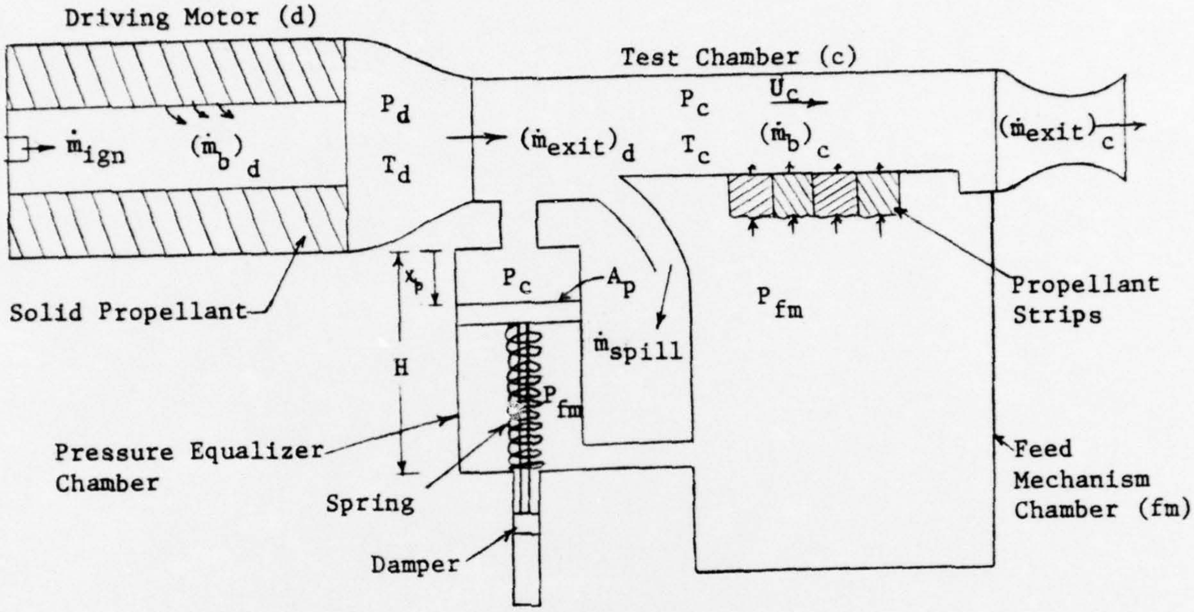

Fig. B.1 Schematic Diagram Showing Mass Flow Rates In and Out of Each Chamber of the Test Rig

From Eqs. (B.3) and (B.4), we have

$$\frac{d(Me)}{dt} = C_v \rho T \frac{d\forall}{dt} + \frac{C_v \forall}{R} \frac{dp}{dt} \tag{B.5}$$

Substitute Eqs. (B.4) and (B.5) into Eqs. (B.1) and (B.2) respectively, we have

$$\left\{ \rho \frac{d\forall}{dt} + \frac{\forall}{RT} \frac{dp}{dt} - \frac{\forall \rho}{T} \frac{dT}{dt} \right\}_d = \dot{m}_{ign} + (\dot{m}_b)_d - (\dot{m}_{exit})_d \tag{B.6}$$

$$\left\{ C_v \rho T \frac{d\forall}{dt} + \frac{C_v \forall}{R} \frac{dp}{dt} \right\}_d = \dot{m}_{ign} h_{ign} + (\dot{m}_b C_p T_f)_d - (\dot{m}_{exit} h_{Texit})_d - (\dot{q}_{loss})_d \tag{B.7}$$

In the driving motor, the rate of change of volume is given by the following equation:

$$\left(\frac{d\forall}{dt}\right)_d = (r_b A_b)_d \tag{B.8}$$

Multiply Eq. (B.6) by $(C_v T)_d$ and subtract from Eq. (B.7), and use Eq. (B.8), we finally get

$$\left(\frac{dT}{dt}\right)_d = \left(\frac{\gamma-1}{\rho R \forall}\right)_d \Big[(\dot{m}_{ign} h_{ign}) + (\dot{m}_b C_p T_f)_d - (\dot{m}_{exit} h_{Texit})_d$$

$$- (\dot{q}_{loss})_d - \left\{ \dot{m}_{ign} + \dot{m}_b - \dot{m}_{exit} \right\}_d \left(\frac{R}{\gamma-1}\right)_d T_d \Big] \tag{B.9}$$

$$\left(\frac{dp}{dt}\right)_d = \left\{\frac{J(\gamma-1)}{\forall}\right\}_d \Big[\dot{m}_{ign} h_{ign} + (\dot{m}_b C_p T_f)_d - (\dot{m}_{exit} h_{Texit})_d - (\dot{q}_{loss})_d$$

$$- \left(\frac{R\rho}{\gamma-1}\right)_d (r_b A_b T)_d \Big] \tag{B.10}$$

Mass balance in the test chamber:

$$\left(\frac{dM}{dt}\right)_c = (\dot{m}_{exit})_d + (\dot{m}_b)_c - (\dot{m}_{exit})_c - (\dot{m}_{spill})_c \tag{B.11}$$

Energy balance in the test chamber:

$$\left\{\frac{d(Me)}{dt}\right\}_c = (\dot{m}_{exit}\, h_{T_{exit}})_d + (\dot{m}_b C_p T_f)_c - (\dot{m}_{exit}\, h_{T_{exit}})_c - (\dot{m}_{spill}\, h_{T_{spill}})_c - (\dot{q}_{loss})_c \tag{B.12}$$

The subscript c refers to the test chamber. A simplification of Eqs. (B.11) and (B.12) similar to that followed earlier for the driving motor results in the following equations:

$$\left(\frac{dT}{dt}\right)_c = \left(\frac{\gamma-1}{\rho R \forall}\right)_c \Big[(\dot{m}_{exit}\, h_{T_{exit}})_d + (\dot{m}_b C_p T_f)_c - (\dot{m}_{exit}\, h_{T_{exit}})_c - (\dot{m}_{spill}\, h_{T_{spill}})_c$$

$$- (\dot{q}_{loss})_c - \left\{ (\dot{m}_{exit})_d + (\dot{m}_b)_c - (\dot{m}_{exit})_c - (\dot{m}_{spill})_c \right\} \left(\frac{R}{\gamma-1}\right)_c T_c \Big] \tag{B.13}$$

$$\left(\frac{dp}{dt}\right)_c = \left\{\frac{J(\gamma-1)}{\forall}\right\}_c \Big[(\dot{m}_{exit}\, h_{T_{exit}})_d + (\dot{m}_b C_p T_f)_c - (\dot{m}_{exit}\, h_{T_{exit}})_c - (\dot{m}_{spill}\, h_{T_{spill}})_c$$

$$- (\dot{q}_{loss})_c - \left(\frac{R\rho}{\gamma-1}\right)_c \left(\frac{d\forall}{dt}\right)_c T_c \Big] \tag{B.14}$$

In Eqs. (B.9) - (B.10) and Eqs. (B.13) - (B.14), $\dot{m}_{exit}$, and $h_{T_{exit}}$ are calculated by the following equations:

$$\dot{m}_{exit} = C_d A_{exit}\, \rho \sqrt{2 g J C_p T \left\{ \left(\frac{p_{exit}}{p}\right)^{\frac{2}{\gamma}} - \left(\frac{p_{exit}}{p}\right)^{\frac{1+\gamma}{\gamma}} \right\}} \tag{B.15}$$

$$h_{T_{exit}} = C_p T + \frac{U^2}{2gJ} \tag{B.16}$$

Eq. (B.15) is based on the assumption of isentropic flow in a nozzle.

We can also write for the volume in the test chamber,

$$\forall_c = (\forall_o)_c + A_p x_p \tag{B.17}$$

$$\frac{d\forall_c}{dt} = A_p u_p \tag{B.18}$$

where $(\forall_o)_c$ is the volume of the test chamber when $x_p = 0$ (see Fig. B.1). u_p and x_p depend on the pressure difference across the piston. The pressure equalizer chamber consists of 2 cylinders. Each cylinder contains a piston, a spring and a damper. A force balance for the piston, spring and damper system within a single cylinder gives the following equations:

$$\frac{du_p}{dt} = \frac{1}{m_p}\left[(P_c - P_{fm}) A_p - d_c u_p - s_k x_p\right] \tag{B.19}$$

$$\frac{dx_p}{dt} = u_p \tag{B.20}$$

where m_p is the piston mass, d_c is the damping factor, s_k is the spring constant. To evaluate P_{fm} , we assume a polytropic compression of the gas in the feed mechanism chamber. Therefore, we have

$$P_{fm} = (P_{fm})_o \left[\frac{(\forall_o)_{fm} + A_p H n_c}{(\forall_o)_{fm} + (H - x_p) A_p n_c}\right]^n \tag{B.21}$$

where $(\forall_o)_{fm}$ is the volume in the feed mechanism chamber excluding the free volume in cylinders, $(P_{fm})_o$ is the initial pressure, n is the exponent in the polytropic compression, and n_c is the number of cylinders.

Surface temperature of propellant strips in the test chamber is given by the following equation.*

$$\left(\frac{dT_{ps}}{dt}\right)_c = \frac{4\alpha_s h_{conv}^2 (T_c - T_{ps})^3}{3\lambda_s^2 (T_{ps} - T_{pi})(2T_c - T_{ps} - T_{pi})} \tag{B.22}$$

---

*This equation is derived from the transient, one-dimensional heat conduction equation in solid propellant (see reference 37).

where h_{conv} is given by the Dittus Boelter relation:

$$h_{conv} = 0.0295 \left(\frac{\lambda}{L}\right) \left(\frac{\rho U L}{\mu}\right)^{0.8} P_r^{\frac{1}{3}}$$

T_{ps} is assumed constant after it has equalled the ignition temperature.

Eqs. (B.8) - (B.10), (B.13) - (B.14), and (B.18) - (B.22) have been solved on the computer using fourth order Hamming's Modified Predictor-Corrector Scheme. The properties used in the calculations are listed in Table B.I. A parametric study has been performed to determine the effect of various geometric inputs on the gas dynamic properties: pressure, temperature, velocity, etc., in the test rig. The results of these calculations have been plotted and shown in Figs. B.2 - B.7.

Conclusions drawn from the parametric study are:

1. Various gas velocities (0-250 m/sec) and various pressures (up to 300 atm) can be achieved in the test chamber by controlling exit nozzle area (see Figs. B.4 and B.5).
2. Velocity can also be controlled by the variation of height in test chamber (see Fig. B.6).
3. Mass flux and velocity in the test chamber can be changed by using different burning surface area of propellant in the driving motor (see Fig. B.5 and B.7).
4. Steady state conditions for pressure, temperature, and velocity can be achieved in the test chamber after a very short transient interval (see Figs. B.2 and B.3).

TABLE B.I.

Properties Used in Parametric Studies

$(W)_d = 22.01$ Kg/Kg-mole

$(W)_c = 22.01$ Kg/Kg-mole

$(\rho_s)_d = 1.6 \times 10^{-3}$ Kg/cm^3

$(\rho_s)_c = 1.6 \times 10^{-3}$ Kg/cm^3

$(\alpha_s)_c = 1.875 \times 10^{-3}$ cm^2/sec

$(\lambda_s)_c = 9.0 \times 10^{-7}$ Kcal/cm-°K-sec

$\mu_c = (2.5 \times 10^{-8} + 4.333 \times 10^{-10} T_c)$ Kg/cm-sec

$(T_{ign})_c = 700$°K

$T_{pi} = 298$°K

$(C_p)_d = 0.35$ Kcal/Kg-°K

$(C_p)_c = 0.35$ Kcal/Kg-°K

$(r_b)_c = a\ p^n + \frac{\alpha G^{0.8}}{x^{0.2}} \text{Exp}\ (- \frac{\beta\ r_b\ \rho_s}{\rho U_\infty})$, Lenoir-Robillard[12] Equation

$\alpha = 6.129$ cm$^{2.8}$/sec$^{0.2}$Kg$^{0.8}$

$\beta = 105$

$(r_b)_d = a\ p^n$

$a = 8.812 \times 10^{-2}$

$n = 0.542$

$(T_f)_d = 2298$°K

$(T_f)_c = 2225$°K

$P_r = 1.0$

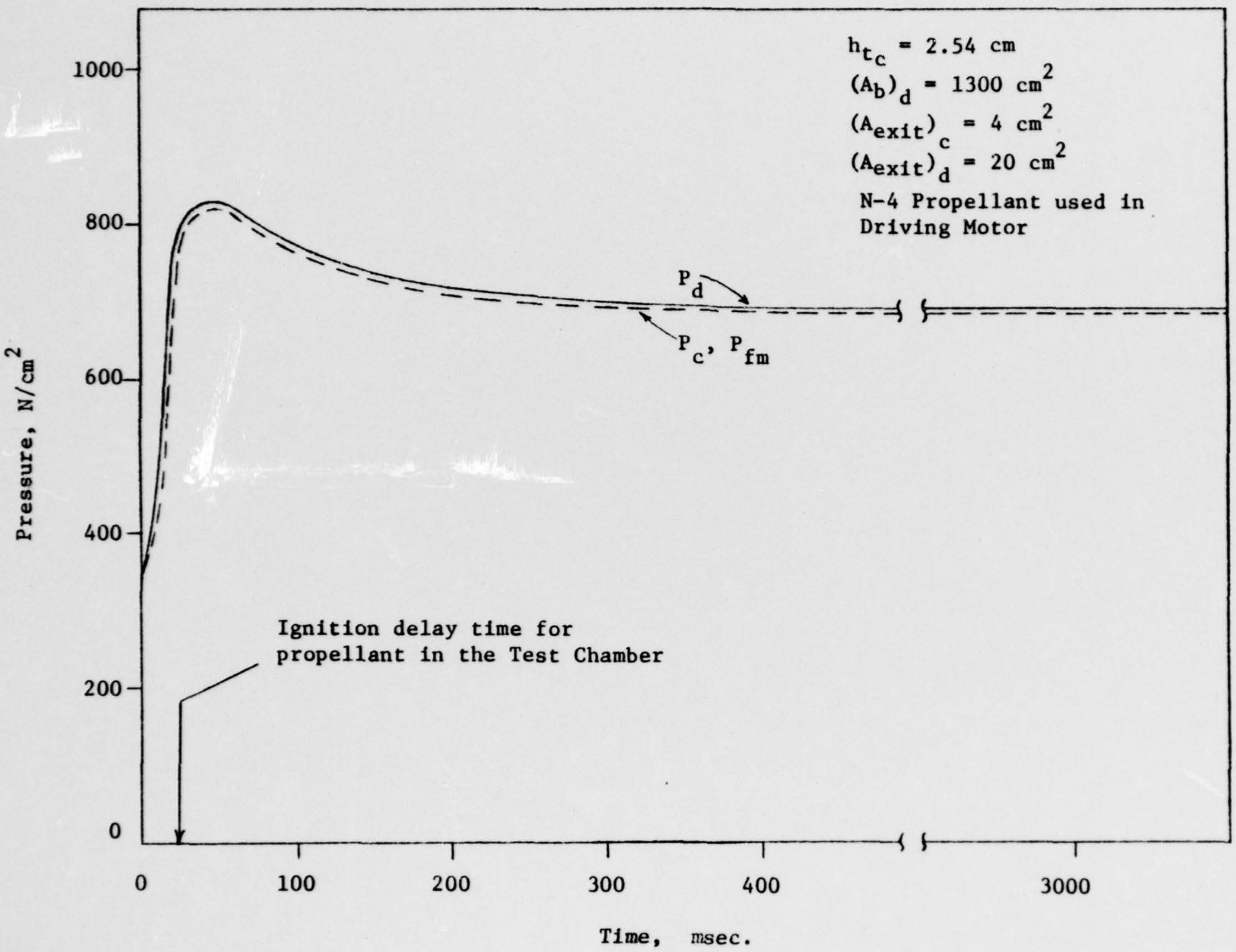

Fig. B.2 Calculated Pressure-Time Traces in the Test Rig

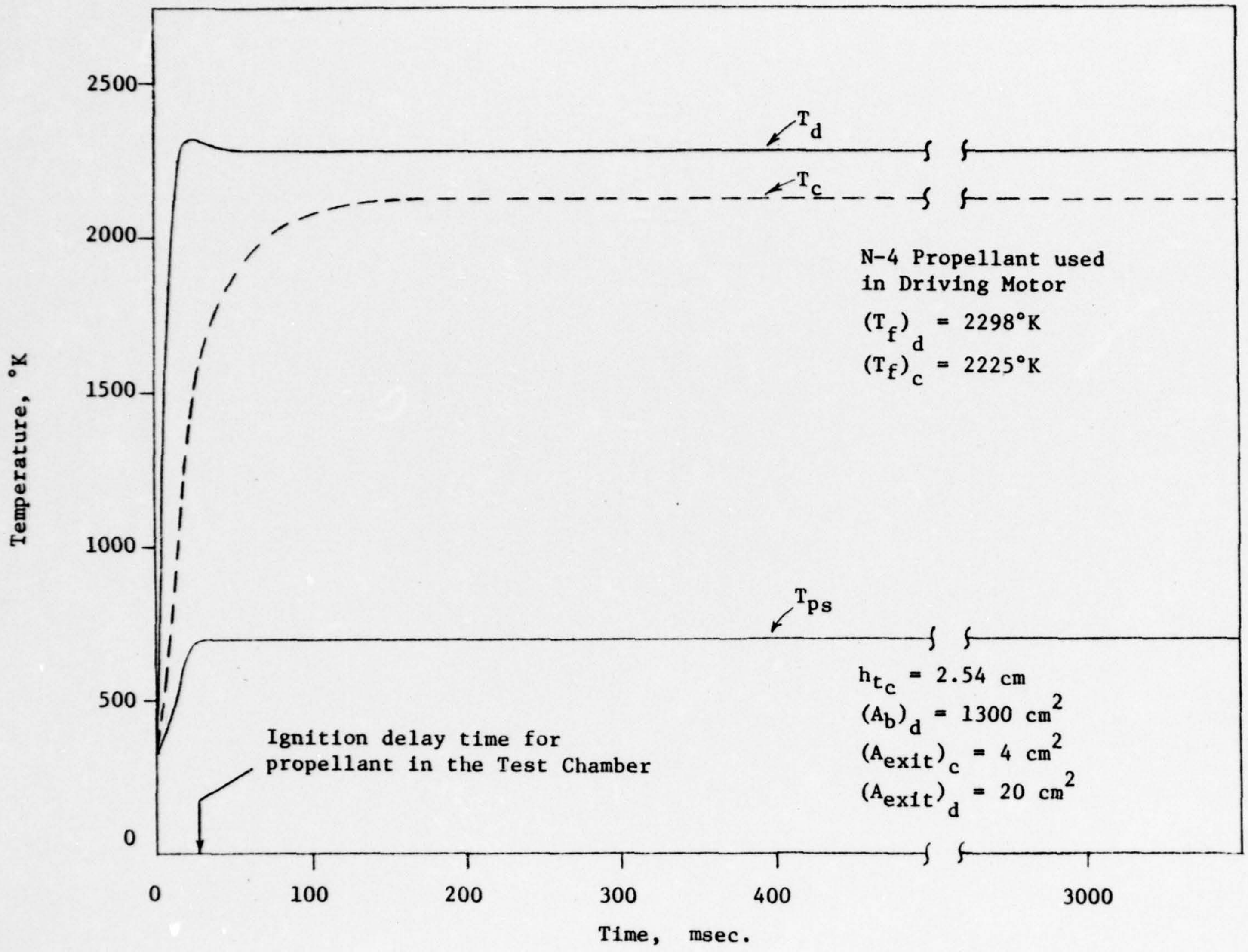

Fig. B.3 Calculated Temperature-Time Traces in the Test Rig

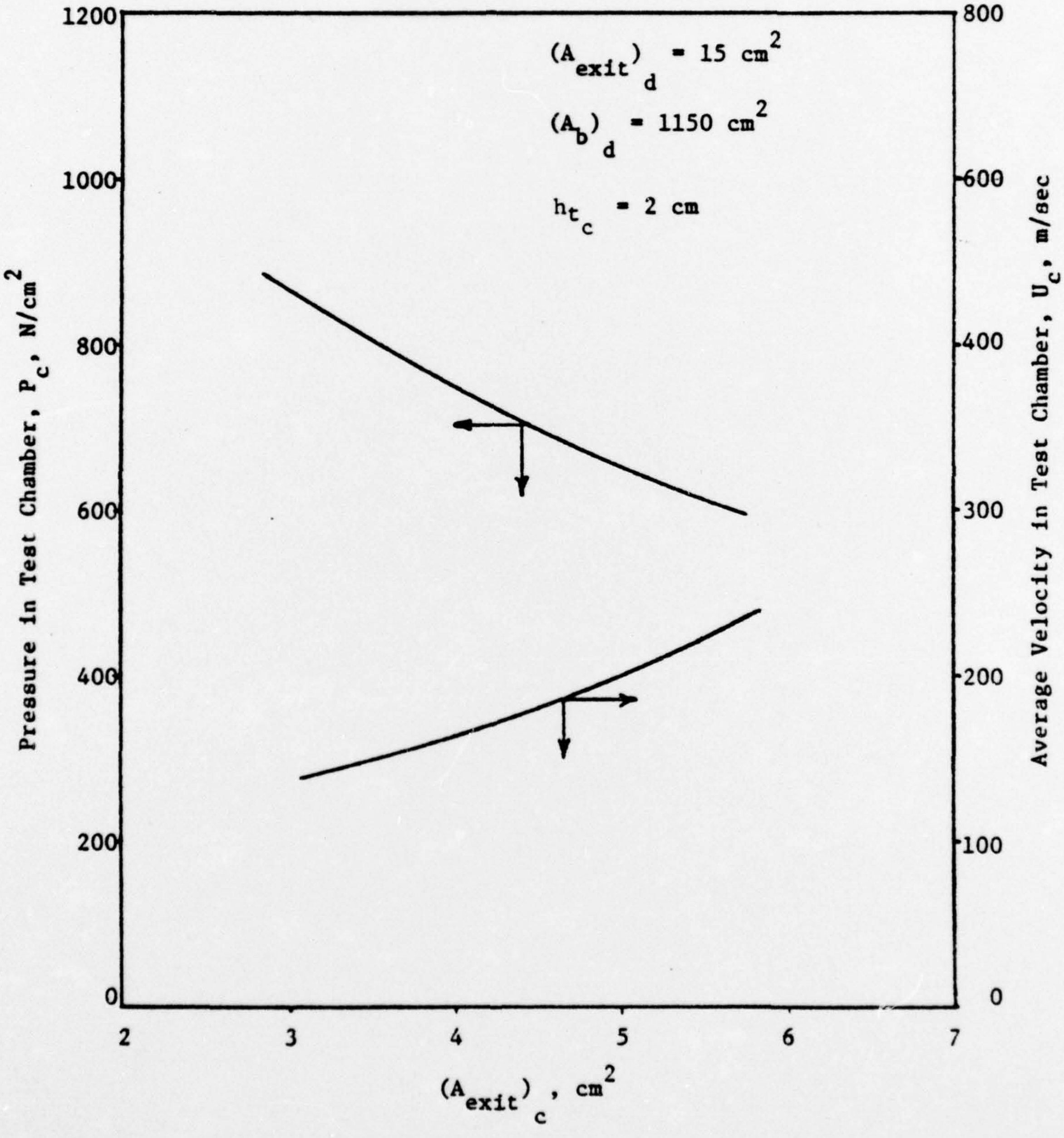

Fig. B.4 Effect of Test Chamber Exit Area on Pressure and Velocity in the Test Chamber (Calculation is based N-4 Propellant in the Driving Motor)

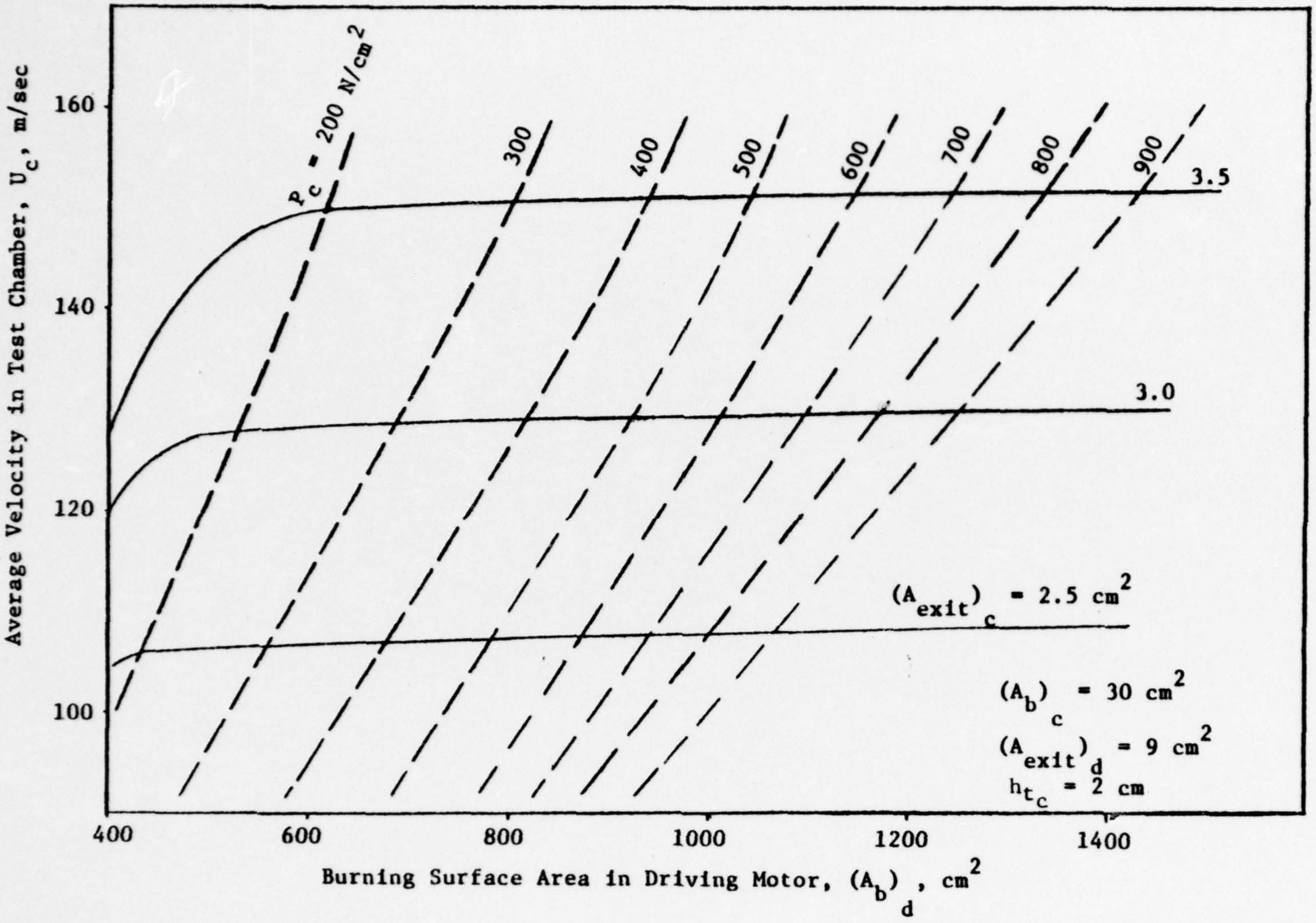

Fig. B.5 **Effect of Burning Surface Area in Driving Motor and** Exit Area on the Velocity and Pressure in the Test Chamber

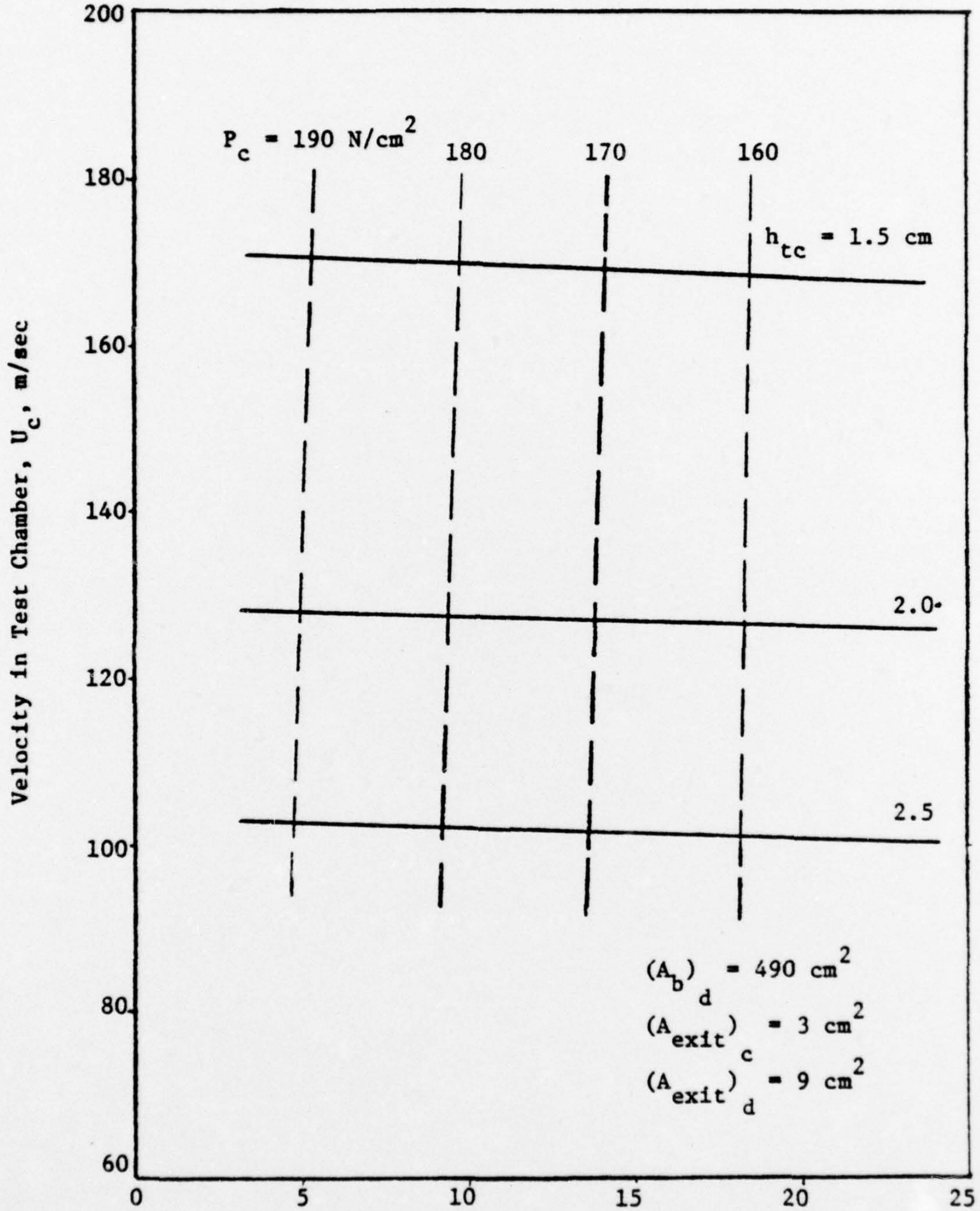

Fig. B.6 Effect of Test Chamber Height and Spillage on the Velocity and Pressure in the Test Chamber

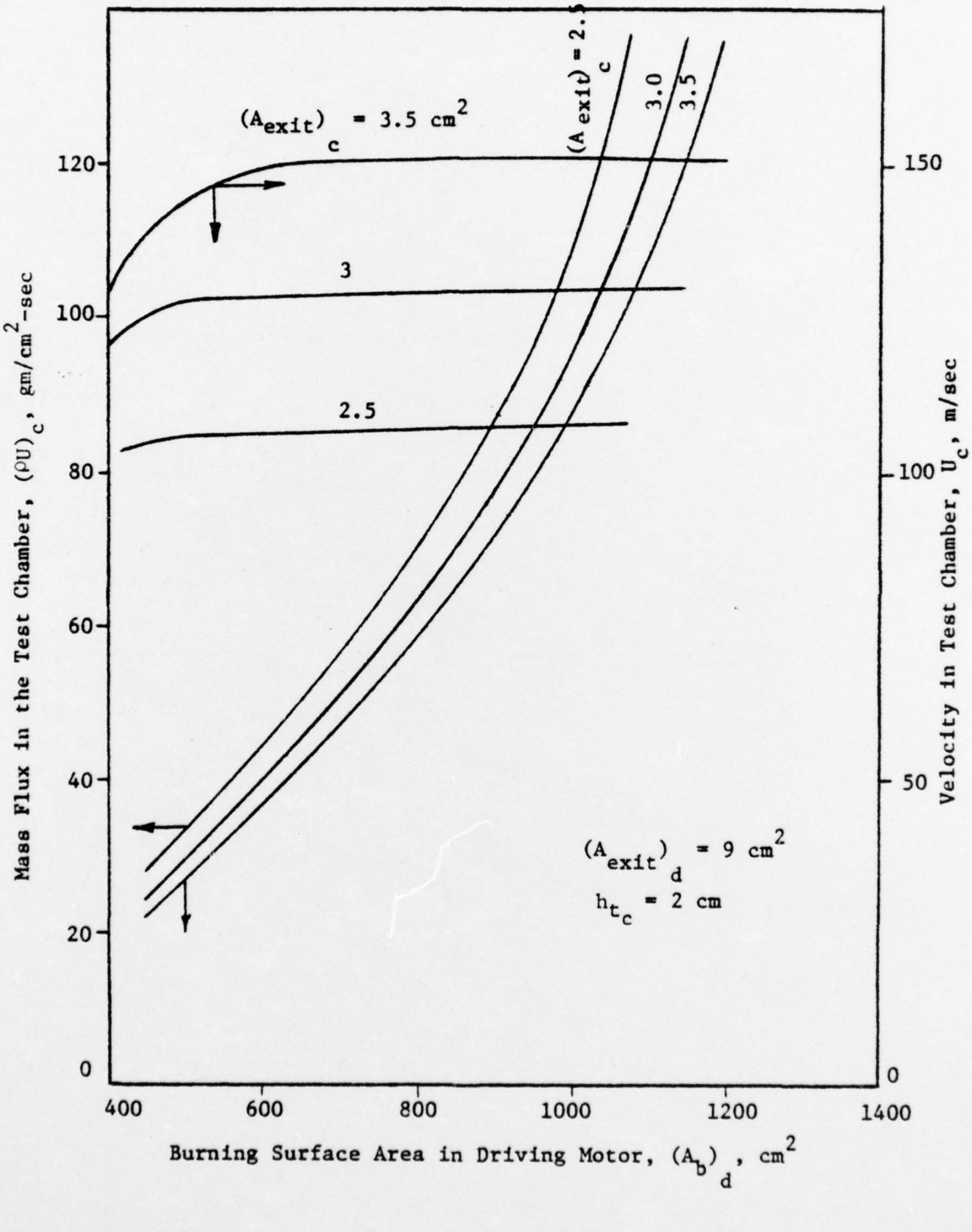

Fig. B.7 Effect of Burning Area in Driving Motor and Exit Area on the Mass Flux and Velocity

UNCLASSIFIED

SECURITY CLASSIFICATION OF THIS PAGE (*When Data Entered*)

REPORT DOCUMENTATION PAGE

READ INSTRUCTIONS
BEFORE COMPLETING FORM

1. REPORT NUMBER
AFOSR - TR- 76 - 1424

2. GOVT ACCESSION NO.

3. RECIPIENT'S CATALOG NUMBER

4. TITLE (*and Subtitle*)
EROSIVE BURNING STUDIES OF COMPOSITE SOLID PROPELLANTS BY THE REACTING TURBULENT BOUNDARY-LAYER APPROACH

5. TYPE OF REPORT & PERIOD COVERED
INTERIM
1 Aug 75 - 30 Sep 76

6. PERFORMING ORG. REPORT NUMBER

7. AUTHOR(s)
MOHAN K RAZDAN
KENNETH K KUO

8. CONTRACT OR GRANT NUMBER(s)
AFOSR-76-2914 new

9. PERFORMING ORGANIZATION NAME AND ADDRESS
THE PENNSYLVANIA STATE UNIVERSITY
DEPARTMENT OF MECHANICAL ENGINEERING
UNIVERSITY PARK, PENNSYLVANIA 16802

10. PROGRAM ELEMENT, PROJECT, TASK AREA & WORK UNIT NUMBERS
~~681308~~
9711-01
61102F

11. CONTROLLING OFFICE NAME AND ADDRESS
AIR FORCE OFFICE OF SCIENTIFIC RESEARCH/NA
BLDG 410
BOLLING AIR FORCE BASE, D C 20332

12. REPORT DATE
Nov 76

13. NUMBER OF PAGES
81

14. MONITORING AGENCY NAME & ADDRESS(*if different from Controlling Office*)

15. SECURITY CLASS. (*of this report*)
UNCLASSIFIED

15a. DECLASSIFICATION/DOWNGRADING SCHEDULE

16. DISTRIBUTION STATEMENT (*of this Report*)

Approved for public release; distribution unlimited.

17. DISTRIBUTION STATEMENT (*of the abstract entered in Block 20, if different from Report*)

18. SUPPLEMENTARY NOTES

19. KEY WORDS (*Continue on reverse side if necessary and identify by block number*)
EROSIVE BURNING
REACTIVE TURBULENT BOUNDARY LAYER
LASER-PHOTODIODE SERVOMECHANISM

20. ABSTRACT (*Continue on reverse side if necessary and identify by block number*)

The overall objective of the current research is to achieve a basic understanding of the erosive burning mechanism in solid-propellant rocket motors. Both theoretical and experimental studies are undertaken. In the theoretical modeling, a reactive turbulent boundary-layer approach is used to analyze the erosive burning phenomenon. A second-order turbulent closure has been selected in the theoretical formulation. The theoretical model can be used to study the effect of gas velocity, pressure, streamwise pressure gradient, oxidizer particle size, and oxidizer-to-fuel ratio. For model validation, a test rig has been designed

over

DD FORM 1 JAN 73 1473 EDITION OF 1 NOV 65 IS OBSOLETE

UNCLASSIFIED

SECURITY CLASSIFICATION OF THIS PAGE (*When Data Entered*) to establish a two-dimensional, turbulent boundary layer flow over a flat plate. The test rig can operate under various gas-dynamic conditions. A laser-photodiode servomechanism has been developed to measure the burning rate, and preliminary tests have demonstrated successful operation of the apparatus.